Title

McrD binds asymmetrically to methyl-coenzyme M reductase improving active site accessibility during assembly

Authors

Grayson L. Chadwick[1,*,†], Aaron M.N. Joiner[1,†], Sangeetha Ramesh[2,3], Douglas A. Mitchell[2,3,4], Dipti D. Nayak[1,*]

Affiliation

Department of Molecular and Cell Biology, University of California, Berkeley, CA, USA[1,] Department of Microbiology, University of Illinois, Urbana, Illinois, USA[2], Carl R. Woese Institute for Genomic Biology, University of Illinois, Urbana, Illinois, USA[3], Department of Chemistry, University of Illinois, Urbana, Illinois, USA[4]

One-sentence summary

Structural characterization of methyl-coenzyme M reductase assembly intermediates.

***To whom correspondence should be addressed:**

Grayson L. Chadwick (chadwick@berkeley.edu), Department of Molecular and Cell Biology, 1 Barker Hall, University of California, Berkeley, CA 94720-3204

Dipti D. Nayak (dnayak@berkeley.edu), Department of Molecular and Cell Biology, 1 Barker Hall, University of California, Berkeley, CA 94720-3204; Tel +1-510-664-5267

[†]These authors contributed equally to this work.

ABSTRACT

Methyl-coenzyme M reductase (MCR) catalyzes the formation of methane and its activity accounts for nearly all biologically produced methane released into the atmosphere. The assembly of MCR is an intricate process involving the installation of a complex set of post-translational modifications and the unique Ni porphyrin cofactor F_{430}. Despite decades of research, details of MCR assembly remain largely unresolved. Here, we report the structural characterization of MCR in two intermediate states of assembly. These intermediate states lack one or both F_{430} cofactors and form complexes with the previously uncharacterized McrD protein. McrD is found to bind asymmetrically to MCR, displacing large regions of the alpha subunit and increasing active site accessibility for the installation of F_{430}—shedding light on the assembly of MCR and the role of McrD therein. This work offers crucial information for the expression of MCR in a heterologous host and provides new targets for the design of MCR inhibitors.

Main text

Methyl-coenzyme M reductase (MCR) is the enzyme responsible for nearly all biological methane production and is found exclusively in the domain Archaea. MCR is a C2-symmetric heterohexamer defined by $\alpha_2\beta_2\gamma_2$ subunit stoichiometry (**fig. S1A**). Substrate tunnels lined with post-translational modifications (PTMs) end in two active sites formed at the interface of the α, α', β and γ subunits and α', α, β' and γ' on the opposing side (**fig. S1B-C**). Each active site contains F_{430}, a unique Ni porphinoid that catalyzes the reduction of methyl-coenzyme M (CH_3-CoM) by coenzyme B (CoB), yielding methane and a heterodisulfide (*1*) (**fig. S1D**). Subsequent studies have determined MCR structures from diverse methanogens (*2*), mutants lacking specific substrate channel PTMs (*3*, *4*), anaerobic methanotrophic (ANME) archaea, which use the enzyme in the reverse direction for methane oxidation (*5*), and the recently discovered Alkyl-coenzyme M reductases (ACR), which can oxidize short chain alkanes (*6*). Together, this research has facilitated studies on the reaction mechanism of MCR (*7*), and the mode of action for MCR inhibitors used to reduce the emission of this potent greenhouse gas (*8*, *9*).

Despite the advances in our understanding of MCR structure and function, key questions regarding its assembly and activation remain unresolved. For instance, the three subunits αβγ encoded by the *mcrABG* genes are found together in an operon with two additional genes: *mcrC* and *mcrD* (**Fig. 1A**). The function of the McrC and McrD proteins is unknown but they are universally conserved in methanogens and have been suggested to be involved in MCR activation (*10*) and assembly (*11*), respectively. McrD associates with MCR in native organisms (*12*) and when heterologously expressed (*11*), and McrD produced in *E. coli* stimulated the final step of F_{430} biosynthesis(*13*). Based on these observations, McrD is hypothesized to be a chaperone required for the insertion of F_{430} into a previously unobserved apo-MCR (*11*, *14*). Here, we utilize Cas9-based genome editing in *Methanosarcina acetivorans* (*15*) to characterize McrD and employ single-particle cryoelectron microscopy (cryoEM) to visualize McrD-bound MCR assembly intermediates.

Surprisingly, although the entire MCR operon is essential (*16*), the *mcrD* gene is not in *M. acetivorans* (**Fig. 1A**). We generated a Δ*mcrD* mutant and verified the absence of compensatory mutations or off-target editing by whole genome resequencing (**fig. S2**). This Δ*mcrD* strain exhibited only a minor increase in doubling time compared to the parental strain when grown on a variety of substrates (**Fig. 1B**). The growth defect remained negligible in cells stressed by nickel limitation, oxygen exposure and non-ideal growth temperatures (**fig. S3**). Consistent with this minor growth defect, only a small number of genes were significantly differentially expressed in the Δ*mcrD* mutant (**fig. S4**).

We used a tetracycline-inducible expression vector to reintroduce the *mcrD* gene with N-terminal tandem FLAG and Strep tags into the Δ*mcrD* background (**Fig. 1A**). McrD expression was verified by Western blot against the FLAG epitope in crude cell extracts (**fig. S5**). Affinity purification of tagged McrD yielded stoichiometric amounts of McrA, B and G subunits, indicative of a McrABGD complex in *M. acetivorans* (**fig. S6**). This complex is less thermostable and exhibited far less F_{430} absorbance compared to full assembled MCR (*17*) (**fig. S7**). Intriguingly, this complex could only be recovered from actively dividing cells, while purification from cells in stationary phase yielded predominantly free McrD (**fig. S6**). The presence of an McrABGD complex primarily in exponential phase is consistent with its role in

the assembly of MCR rather than in a repair pathway to salvage damaged MCR. Additionally, isolation of the McrABGD complex was insensitive to the location of affinity tags on McrD, suggesting that it forms through a biologically relevant interaction between McrD and the other subunits, not a spurious interaction between the tag and MCR (**fig. S6**).

Two distinct conformational states of the McrABGD complex were discovered by cryoEM: 1) semi-apo at 3Å and 2) apo-apo at 3.1Å (**Fig. 1C, D**, **fig. S8-9**). We docked a previous crystal structure, of the $MCR_{ox1\text{-}silent}$ state purified from *Methanosarcina barkeri* (*2*), along with an AlphaFold2 (*18*, *19*) prediction of McrD into both densities and then manually rebuilt each model. Surprisingly, all of the cryoEM density in both maps could be accounted for by a complex with $\alpha_2\beta_2\gamma_2D_1$ stoichiometry. These asymmetric complexes were supported by a molar mass estimate, acquired by size exclusion chromatography coupled with multi-angle light scattering, of roughly 256kDa, which is too small for $\alpha_2\beta_2\gamma_2D_2$ (~313kDa) and too large for $\alpha_1\beta_1\gamma_1D_1$ (~157kDa) (**fig. S10**). Consistent with the hypothesis that McrD assists in the formation of an assembly intermediate, the two conformations differ in their active site occupancy. Both active sites in the apo-apo model are empty whereas the semi-apo model contains one empty active site and the other one shows clear density corresponding to the presence of three ligands (F_{430}, CoM, and CoB) (**Fig. 1C, D**).

In each conformational state, McrD is nestled between the γ, α and α' subunits (semi-apo lettering, **Fig. 2A**). Residues 10-129 of McrD are resolvable in our cryoEM density and adopt a βαββαβ fold motif. A large loop between the two βαβ repeats of McrD, composed of residues 47-68, extends upwards forming a wedge between the γ and α' subunits, positioning the bulk of McrD in a region normally occupied by the N-terminal domain of the α subunit (**Fig. 2B**). The N-terminal domain of the α subunit bends down and outwards along the β-sheet of McrD, converting $Leu^{\alpha78}$-$Arg^{\alpha81}$ into a β-strand (**Fig. 2B**). Although the C-terminus of McrD is partially unresolved in our structures, overlaying the full-length AlphaFold2 prediction reveals that the C-terminal domain contributes to the formation of a small putative tunnel into which the $Leu^{\alpha78}$-$Arg^{\alpha81}$ β-strand fits neatly (**fig. S11**). The formation of this β-strand involves a major reorganization of the N-terminal domain of the α subunit (**Fig. 2C**). In both conformations, binding of McrD results in large-scale movements of γ and β compared to previous crystal structures (**Fig 2D**), resulting in increased accessibility of the active site on the McrD-bound side. The resolution of the cryoEM structures was sufficient to visualize the methylations of Arg^{285} and Cys^{472} in α and α' (**Fig. 2E**), which were also detected by high-resolution and tandem mass spectrometry (HRMS/MS) (**fig. S12-S14**). The didehydro Asp^{470}, thio Gly^{465} and *N*-methyl His^{271} modifications were detected and verified by HRMS/MS despite ambiguity in the cryoEM data (**Fig. 2F**).

The asymmetric nature of these structures results in four unique active site conformations (**Fig. 3A,B**). In both models, the active site on the McrD-bound side is the most distorted compared to the crystal structure of fully assembled MCR (**Fig. 3C, S15A**). Nearly all active site forming secondary structures deviate significantly and are unresolvable in some places, most notably the loops between $Leu^{\alpha333}$-$Tyr^{\alpha346}$ and $Ala^{\alpha158}$-$Glu^{\alpha166}$ containing the F_{430} axial ligand $Gln^{\alpha161}$. The loop between $Asp^{\alpha414}$ and $Phe^{\alpha416}$ show a dramatic rearrangement, with $His^{\alpha415}$ and $Phe^{\alpha416}$ moving in to occupy regions normally filled by F_{430} and the axial ligand loop. Additional

structural changes include a distortion to the loop containing $Tyr^{\beta 365}$ resulting in a reorientation of the hydroxy group by 180 degrees.

The contralateral active sites differ significantly between the semi-apo and apo-apo states. In the semi-apo complex, the contralateral active is nearly identical to those observed in the fully assembled crystal structure (**Fig. 3D**). Strong density is present throughout the entire active site cavity, allowing for unambiguous identification of CoM, CoB and F_{430} as well as the loop containing $Gln^{\alpha 161}$. Here, the N-terminal region of the α' subunit caps the active site as in the crystal structure. In stark contrast, the contralateral active site of the apo-apo structure displays weak density for the loop with $Gln^{\alpha 161}$, and lacks distinct density for the ligands and the entire N-terminal domain of the α' subunit (**fig. S15B**). There is also a prominent deformation of the helix-loop-helix region between $Leu^{\alpha' 333}$ and $Tyr^{\alpha' 346}$ that could not be fully resolved. Notably, $Gln^{\alpha 161}$ has shifted ~7Å away from the active site cavity, consistent with a lack of F_{430}. A comparison of the two active sites in the apo-apo model highlights the importance of McrD binding for F_{430} ingress to the active site. The disordered axial ligand loop leads to a solvent-exposed pathway into the active site that is lined with basic residues contributed by both McrD and the β-strand $Leu^{\alpha' 78}$-$Arg^{\alpha' 81}$ (**Fig. 3F**). In contrast, the contralateral active site remains far less accessible due to a surface covered mostly by acidic residues and an axial ligand loop left largely in place.

Based on these data, we propose a model for the assembly of the MCR complex and the role of McrD in this process (**Fig. 4**). Our model begins with a PTM-containing apo-$\alpha_2\beta_2\gamma_2$ MCR that is folded except for the α subunit N-terminal domains. McrD is not needed to destabilize the α N-terminal domains, as evidenced by the unstructured contralateral N-terminus in our apo-apo $\alpha_2\beta_2\gamma_2D_1$ structure. Free McrD recognizes one of the unfolded N-terminal domains to bind to the complex, yielding our observed apo-apo $\alpha_2\beta_2\gamma_2D_1$ state. Though they have never been visualized, there are two hypothetical ways that assembly might proceed: 1) the association of a second McrD on the contralateral side leading to an apo-apo $\alpha_2\beta_2\gamma_2D_2$ complex, or 2) the insertion of F_{430}, dissociation of McrD, and folding of the alpha N-terminal domain to cap the active site producing a semi-apo $\alpha_2\beta_2\gamma_2$ state. While our purification strategy would never capture the latter state, it should have trapped the former, if present in significant quantities. In the first case, F_{430} insertion followed by McrD loss, or in the second case, rebinding of McrD to the opposite side, would lead to our observed semi-apo $\alpha_2\beta_2\gamma_2D_1$. From here, an additional round of F_{430} insertion, loss of McrD, and folding of the alpha N-terminal domain to cap the active site would yield a conformation identical to the crystallized $MCR_{ox1\text{-}silent}$ form, which is ready to be a substrate for the activation complex.

Here we have provided the first structural insight into the assembly of MCR and McrD's role therein. Similar to the PTMs on the alpha subunit (*3*), the loss of McrD has little if any growth penalty under a variety of laboratory conditions, highlighting that important facets of MCR biology in nature not captured by ideal laboratory conditions. Despite this, our structural insight into empty MCR active sites could propel the design of novel anti-methanogen compounds to block F_{430} insertion. Potent compounds that inhibit MCR, particularly as additives to ruminant feedstocks (*20*), will likely be a reliable and cost-effective strategy to curb methane emissions, which is a critical aspect of international efforts to limit global temperature rise. A complete understanding of the MCR enzyme's assembly, activation and reaction mechanism is crucial for

the development and deployment of diverse classes of MCR antagonists. Furthermore, elucidating the process of MCR assembly and activation advances the biotechnological goal of heterologous expression of the methane generating metabolic pathway, and contributes to our comprehension of the evolutionary transitions required for the natural horizontal transfer of this metabolism (*21*). Future work must identify what additional cellular factors, if any, associate with the McrD-bound assembly intermediates to facilitate F_{430} insertion and N-terminal domain folding.

Materials and Methods

See supplemental information.

Acknowledgements

Funding list for DDN: Beckman Young Investigator Award sponsored by the Arnold and Mabel Beckman Foundation, Searle Scholars Program sponsored by the Kinship Foundation, the Rose Hills Innovator Grant, the Packard Fellowship in Science and Engineering sponsored by the David and Lucille Packard Foundation, and the Simons Early Career Investigator in Marine Microbial Ecology and Evolution Grant sponsored by the Simons Foundation. DDN is a Chan Zuckerberg Biohub Investigator. GLC and AMNJ are supported by the Miller Institute for Basic Research in Science, University of California Berkeley. This work was supported in part by a grant from the National Institutes of Health (GM097142 to D.A.M.).

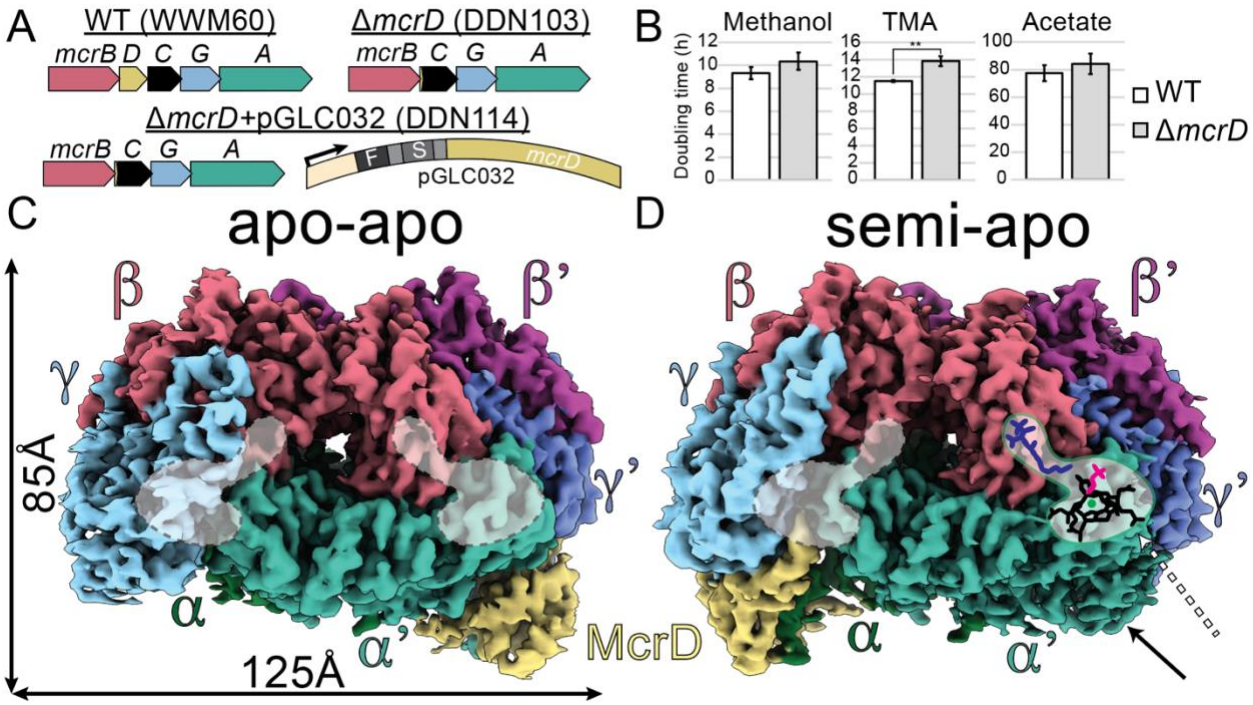

Fig. 1 Construction of Δ*mcrD* strain and cryoEM structure of McrD-bound MCR complexes. (**A**) MCR operon in the parental strain (WWM60), Δ*mcrD* mutant (DDN103), and tagged complementation strain (DDN114). Arrow indicates pMcrB(tetO1) promoter used for tetracycline inducible expression of McrD, F and S represent FLAG and Strep tags, respectively. (**B**) Doubling times of WT and Δ*mcrD* strain on methanol (MeOH), trimethylamine (TMA) and acetate (** p-value < 0.01, two-sided t-test). (**C**, **D**) CryoEM densities of the apo-apo and semi-apo McrABGD complexes (**Supplementary Table 4)**. Empty active sites are outlined with dotted lines, while filled active site on the contralateral side of the semi-apo model is indicated by the dashed arrow. Solid arrow indicates density corresponding to the N-terminal domain of the α' subunit in the semi-apo complex that is absent in the apo-apo complex.

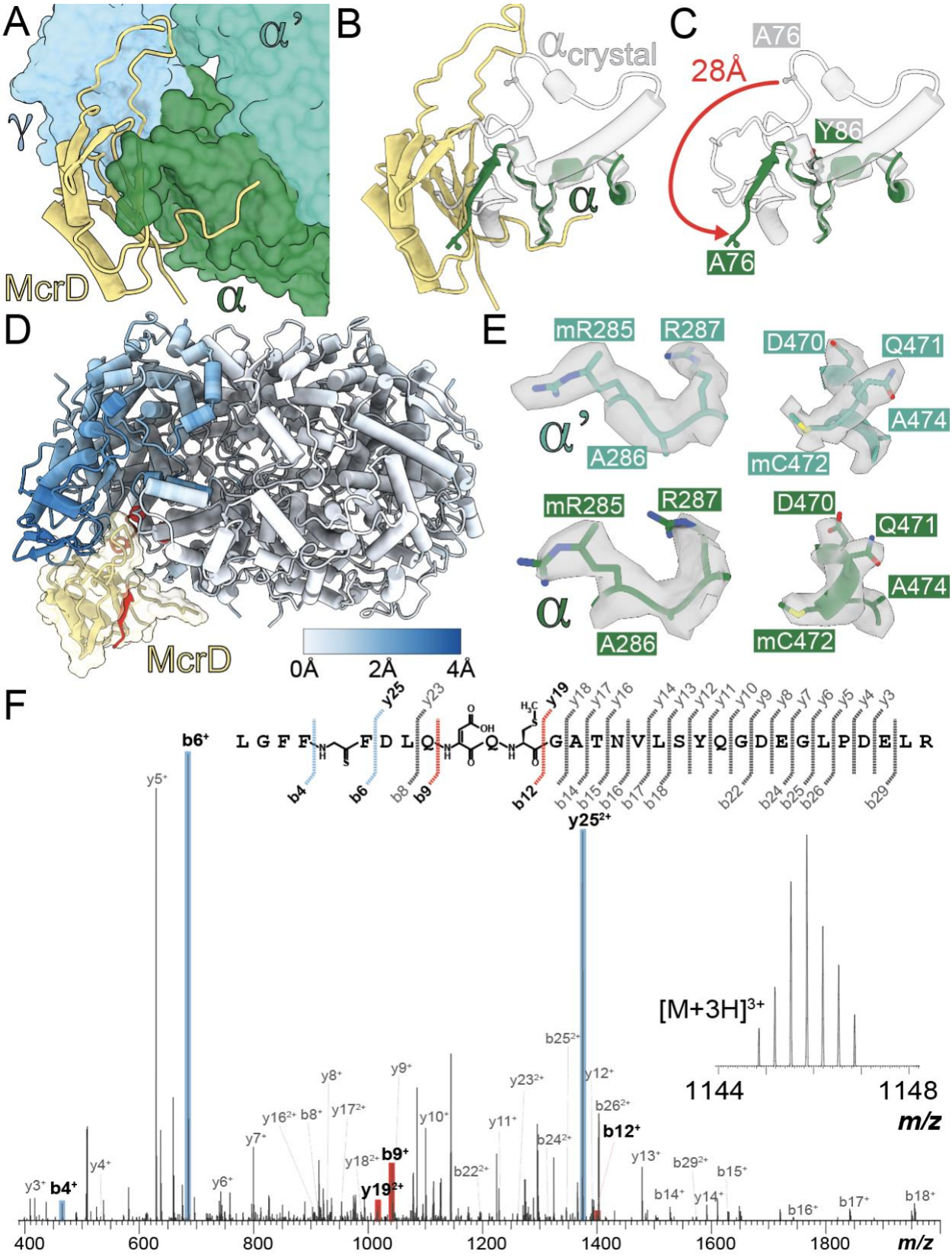

Fig. 2 McrD-binding to PTM-bearing MCR causes large-scale structural changes. (**A**) Detail of McrD binding location on the semi-apo model. (**B**) The α subunit N-terminal domain from the *M. barkeri* MCR crystal structure

(PDB:1e6y) depicted in white, with the corresponding region of the semi-apo α subunit dark green. (**C**) Significant rearrangement exemplified by $Ala^{\alpha 76}$ which deviates 28Å upon McrD binding. All residues before $Ala^{\alpha 76}$ are disordered. (**D**) Ribbon diagram of semi-apo structure colored by Cα deviations from 1e6y. Residues deviating by more than the color scale maximum of 4Å are shown in red. (**E**) Density corresponding to methylations at Arg^{285} and Cys^{472} in the α and α' subunits. (**F**) HRMS/MS fragmentation and annotated collision-induced dissociation spectrum of an McrA tryptic peptide (Leu^{461}-Arg^{491}) conclusively identified three of the five PTMs. Cyan and red mass peaks indicate the most diagnostic ions for localizing the modification sites. For additional details and HRMS/MS data confirming the remaining PTMs, see **fig. S12-S14**.

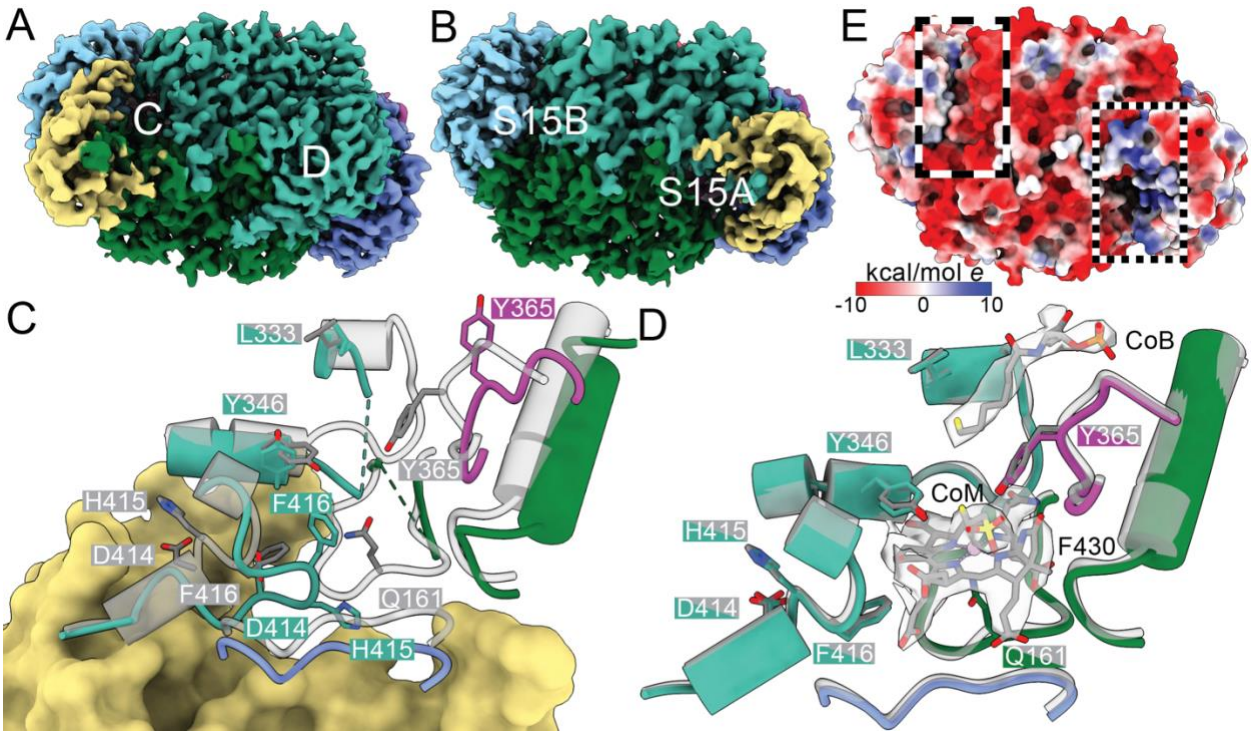

Fig. 3 Active site variations in MCR assembly intermediates. (**A-B**) Bottom view of complexes with labels showing active sites detailed in subsequent panels. (**C-D**) Active site details of the semi-apo model with key residue side chains shown (for corresponding figures for apo-apo model see **fig. S15**). MCR crystal structure from *M. barkeri* (PDB:1e6y) overlaid in gray. In D cryoEM density corresponding to CoM, CoB and F_{430} is shown in transparent gray. (**E**) Bottom view of the apo-apo complex colored by electrostatic potential. Boxed regions on the McrD-bound side (dots) and contralateral side (dashes) highlight strong electrostatic differences, with positively charged patches leading to the active site from McrD and the α' subunit. Boxes indicate similar positions on the side opposite McrD with the axial ligand loop blocking the active site and mostly negatively charged surfaces.

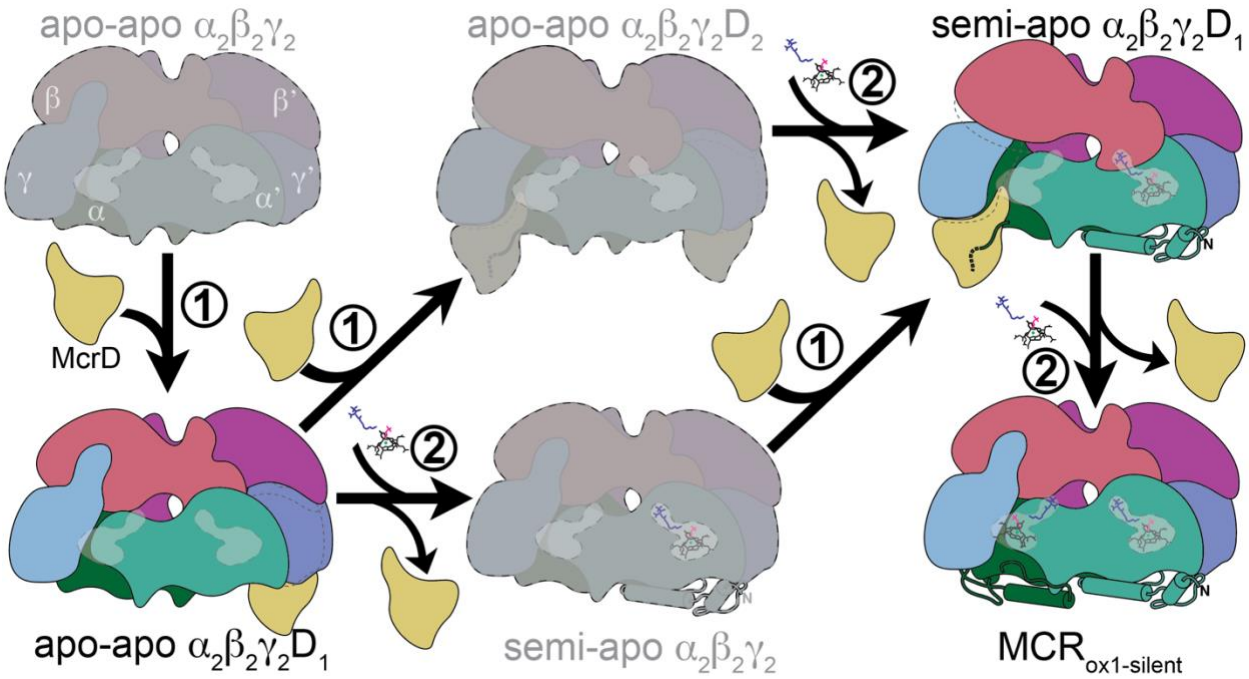

Fig. 4 Role of McrD in MCR assembly. Experimentally observed complexes are shown in full color, while hypothesized intermediates are shown in gray. The two proposed functions of McrD are numbered. 1) McrD recognizes the disordered N-terminal domain of an α subunit lacking F_{430}, and 2) McrD and possibly unidentified additional factors facilitate the insertion of F_{430}, McrD dissociation and α subunit N-terminal domain folding. The order of these two functions is not clear, leading to two possible routes between our observed assembly intermediates.

References

1. U. Ermler, W. Grabarse, S. Shima, M. Goubeaud, R. K. Thauer, Crystal Structure of Methyl-Coenzyme M Reductase: The Key Enzyme of Biological Methane Formation. *Science*. **278**, 1457–1462 (1997).

2. W. Grabarse, F. Mahlert, S. Shima, R. K. Thauer, U. Ermler, Comparison of Three Methyl-coenzyme M Reductases from Phylogenetically Distant Organisms: Unusual Amino Acid Modification, Conservation and Adaptation. *Journal of Molecular Biology*. **303**, 329–344 (2000).

3. D. D. Nayak, A. Liu, N. Agrawal, R. Rodriguez-Carerro, S.-H. Dong, D. A. Mitchell, S. K. Nair, W. W. Metcalf, Functional interactions between posttranslationally modified amino acids of methyl-coenzyme M reductase in Methanosarcina acetivorans. *PLOS Biology*. **18**, e3000507 (2020).

4. D. D. Nayak, N. Mahanta, D. A. Mitchell, W. W. Metcalf, Post-translational thioamidation of methyl-coenzyme M reductase, a key enzyme in methanogenic and methanotrophic Archaea. *eLife*. **6**, e29218 (2017).

5. S. Shima, M. Krueger, T. Weinert, U. Demmer, J. Kahnt, R. K. Thauer, U. Ermler, Structure of a methyl-coenzyme M reductase from Black Sea mats that oxidize methane anaerobically. *Nature*. **481**, 98–101 (2012).

6. C. J. Hahn, O. N. Lemaire, J. Kahnt, S. Engilberge, G. Wegener, T. Wagner, Crystal structure of a key enzyme for anaerobic ethane activation. *Science*. **373**, 118–121 (2021).

7. T. Wongnate, D. Sliwa, B. Ginovska, D. Smith, M. W. Wolf, N. Lehnert, S. Raugei, S. W. Ragsdale, The radical mechanism of biological methane synthesis by methyl-coenzyme M reductase. *Science*. **352**, 953–958 (2016).

8. E. C. Duin, T. Wagner, S. Shima, D. Prakash, B. Cronin, D. R. Yáñez-Ruiz, S. Duval, R. Rümbeli, R. T. Stemmler, R. K. Thauer, M. Kindermann, Mode of action uncovered for the specific reduction of methane emissions from ruminants by the small molecule 3-nitrooxypropanol. *Proceedings of the National Academy of Sciences*. **113**, 6172–6177 (2016).

9. D. Hinderberger, R. P. Piskorski, M. Goenrich, R. K. Thauer, A. Schweiger, J. Harmer, B. Jaun, A Nickel–Alkyl Bond in an Inactivated State of the Enzyme Catalyzing Methane Formation. *Angewandte Chemie International Edition*. **45**, 3602–3607 (2006).

10. D. Prakash, Y. Wu, S.-J. Suh, E. C. Duin, Elucidating the Process of Activation of Methyl-Coenzyme M Reductase. *Journal of Bacteriology*. **196**, 2491–2498 (2014).

11. Z. Lyu, C.-W. Chou, H. Shi, L. Wang, R. Ghebreab, D. Phillips, Y. Yan, E. C. Duin, W. B. Whitman, Assembly of Methyl Coenzyme M Reductase in the Methanogenic Archaeon Methanococcus maripaludis. *Journal of Bacteriology*. **200**, e00746-17 (2018).

12. D. Stroup, J. N. Reeve, Association of the mcrD gene product with methyl coenzyme M reductase in Methanococcus vannielli. *Biochimica et Biophysica Acta (BBA) - Protein Structure and Molecular Enzymology*. **1203**, 175–183 (1993).

13. K. Zheng, P. D. Ngo, V. L. Owens, X. Yang, S. O. Mansoorabadi, The biosynthetic pathway of coenzyme F430 in methanogenic and methanotrophic archaea. *Science*. **354**, 339–342 (2016).

14. R. K. Thauer, Methyl (Alkyl)-Coenzyme M Reductases: Nickel F-430-Containing Enzymes Involved in Anaerobic Methane Formation and in Anaerobic Oxidation of Methane or of Short Chain Alkanes. *Biochemistry*. **58**, 5198–5220 (2019).

15. D. D. Nayak, W. W. Metcalf, Cas9-mediated genome editing in the methanogenic archaeon *Methanosarcina acetivorans*. *Proc. Natl. Acad. Sci. U.S.A.* **114**, 2976–2981 (2017).

16. A. M. Guss, M. Rother, J. K. Zhang, G. Kulkkarni, W. W. Metcalf, New methods for tightly regulated gene expression and highly efficient chromosomal integration of cloned genes for *Methanosarcina* species. *Archaea*. **2**, 193–203 (2008).

17. D. D. Nayak, W. W. Metcalf, "Chapter Thirteen - Genetic techniques for studies of methyl-coenzyme M reductase from Methanosarcina acetivorans C2A" in *Methods in Enzymology*, F. Armstrong, Ed. (Academic Press, 2018; https://www.sciencedirect.com/science/article/pii/S0076687918304269), vol. 613 of *Enzymes of Energy Technology*, pp. 325–347.

18. J. Jumper, R. Evans, A. Pritzel, T. Green, M. Figurnov, O. Ronneberger, K. Tunyasuvunakool, R. Bates, A. Žídek, A. Potapenko, A. Bridgland, C. Meyer, S. A. A. Kohl, A. J. Ballard, A. Cowie, B. Romera-Paredes, S. Nikolov, R. Jain, J. Adler, T. Back, S. Petersen, D. Reiman, E. Clancy, M. Zielinski, M. Steinegger, M. Pacholska, T. Berghammer, S. Bodenstein, D. Silver, O. Vinyals, A. W. Senior, K. Kavukcuoglu, P. Kohli, D. Hassabis, Highly accurate protein structure prediction with AlphaFold. *Nature*. **596**, 583–589 (2021).

19. M. Mirdita, K. Schütze, Y. Moriwaki, L. Heo, S. Ovchinnikov, M. Steinegger, ColabFold: making protein folding accessible to all. *Nat Methods*. **19**, 679–682 (2022).

20. A. N. Hristov, J. Oh, F. Giallongo, T. W. Frederick, M. T. Harper, H. L. Weeks, A. F. Branco, P. J. Moate, M. H. Deighton, S. R. O. Williams, M. Kindermann, S. Duval, An inhibitor persistently decreased enteric methane emission from dairy cows with no negative effect on milk production. *Proceedings of the National Academy of Sciences*. **112**, 10663–10668 (2015).

21. P. S. Garcia, S. Gribaldo, G. Borrel, Diversity and Evolution of Methane-Related Pathways in Archaea. *Annu. Rev. Microbiol.* **76**, 727–755 (2022).

Supplementary Information

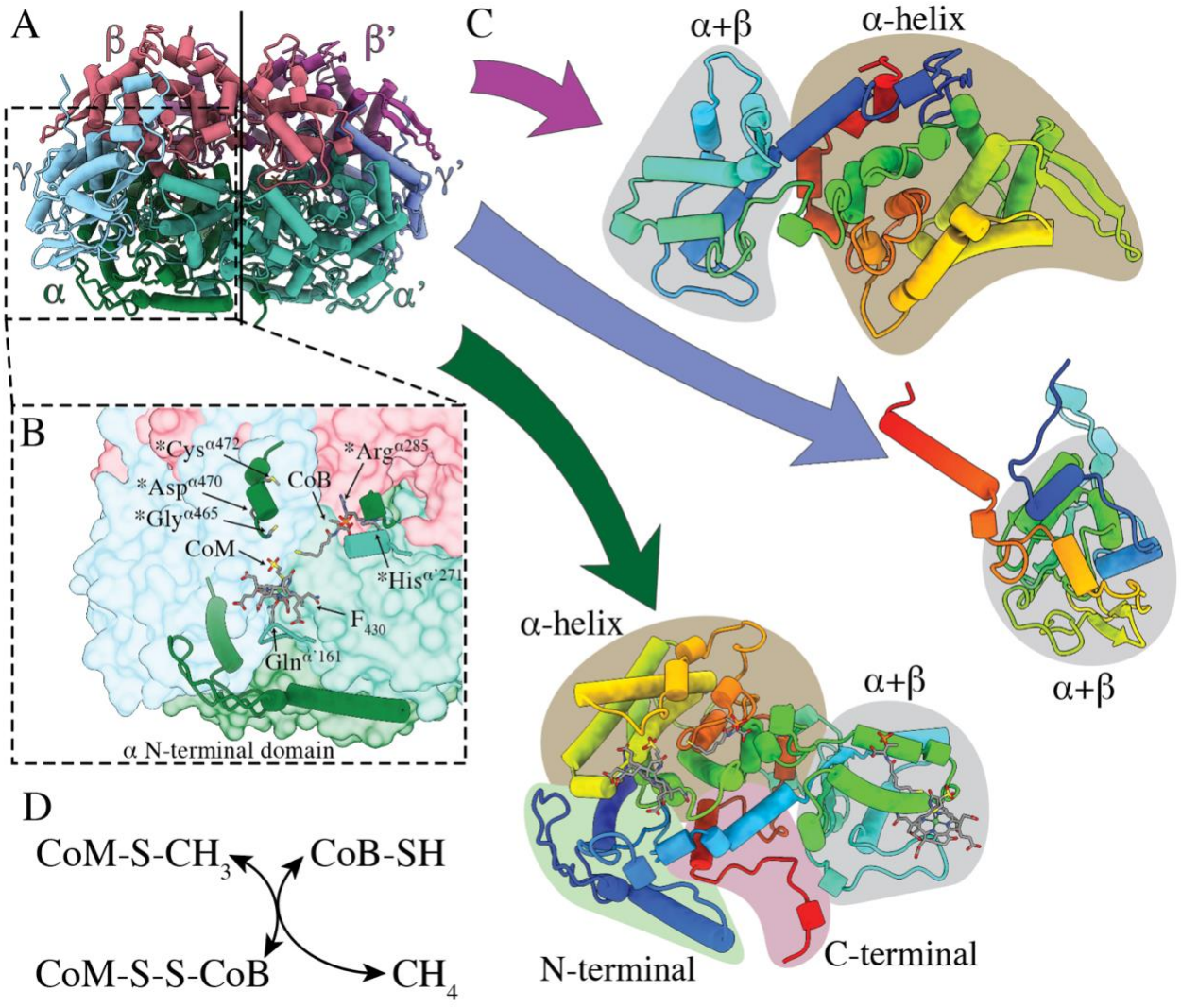

fig. S1 MCR reaction and structural features. (**A**) Crystal structure of methyl-coenzyme M reductase (MCR) from *M. barkeri* demonstrating the quaternary structure of the complex (PDB:1e6y). (**B**) Detail of MCR active site showing coenzyme M (CoM), coenzyme B (CoB), cofactor F_{430}, F_{430}'s axial ligand $Gln^{\alpha'161}$ and the five post-translationally modified residues denoted by asterisks. The N-terminal domain of the α subunit that covers the bottom of active site shown as a cartoon. (**C**) Folds of McrB (top), McrG (right) and McrA (bottom) with major domains labelled as defined by Ermler *et al.* 1997. The α-helix and α+β domains of McrA and McrB are structurally similar, suggesting an ancient duplication event. (**D**) The reversible reaction catalyzed by MCR. Methyl coenzyme M ($CoM\text{-}S\text{-}CH_3$) is reduced by coenzyme B (CoB-SH) to form the heterodisulfide (CoM-S-S-CoB) and methane.

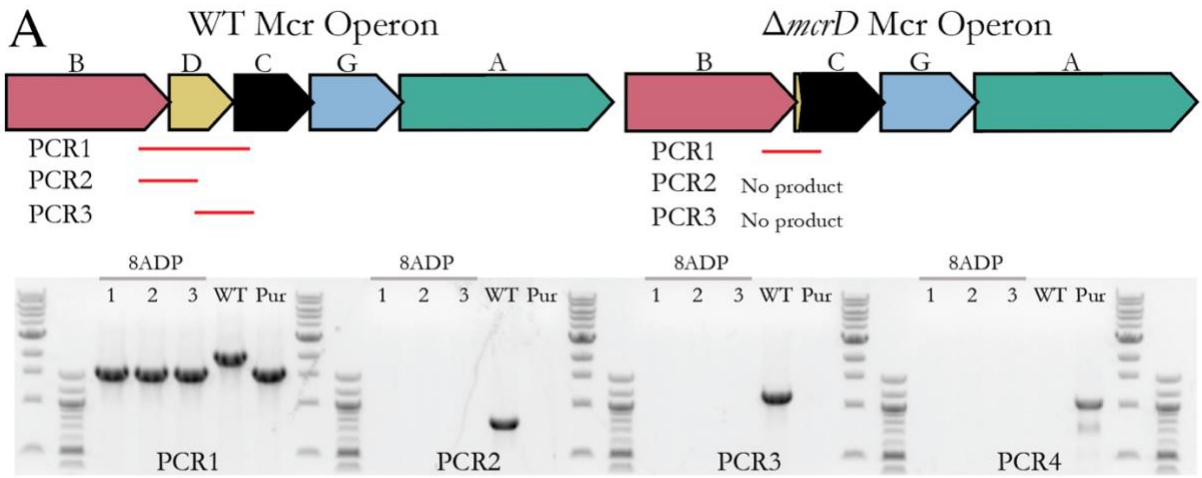

B

Predicted mutations

evidence	position	mutation	annotation	gene	description
RA	487,691	+C	intergenic (+91/-154)	*MA_RS02125* → / → *MA_RS02130*	(4Fe-4S)-binding protein/aldehyde oxidase
RA	941,168	$(A)_{5\rightarrow6}$	coding (27/765 nt)	*MA_RS04205* ←	hypothetical protein
RA	1,314,120	Δ1 bp	pseudogene (467/802 nt)	*MA_RS05790* →	DNA-directed RNA polymerase subunit D
RA	2,086,881	2 bp→CT	intergenic (-200/+180)	*MA_RS09025* ← / ← *MA_RS09030*	cell surface protein/ATPase
RA	2,086,886	G→T	intergenic (-205/+176)	*MA_RS09025* ← / ← *MA_RS09030*	cell surface protein/ATPase
RA	2,534,543	+C	coding (6589/6645 nt)	*MA_RS10645* ←	hypothetical protein
RA	2,836,646	A→G	F64L (TTC→CTC)	*MA_RS11965* ←	phosphoserine aminotransferase
RA	2,867,059	T→G	H313Q (CAT→CAG)	*MA_RS24595* →	hypothetical protein
RA	3,433,201	Δ1 bp	coding (771/774 nt)	*MA_RS14410* →	hypothetical protein
RA	4,295,452	Δ1 bp	intergenic (-25/+484)	*MA_RS24770* ← / ← *MA_RS18150*	hypothetical protein/hypothetical protein
RA	4,874,567	Δ1 bp	intergenic (-82/-693)	*MA_RS20725* ← / → *MA_RS20730*	4Fe-4S ferredoxin/tRNA-Ser
RA	4,945,345	+C	pseudogene (211/1904 nt)	*MA_RS21030* ←	phosphoadenosine phosphosulfate reductase
RA	5,078,585	G→A	M1M (ATG→ATA) †	*MA_RS21710* →	carbamoyltransferase HypF
MC JC	5,599,800	Δ456 bp	coding (31-486/513 nt)	*MA_RS23715* ←	methyl-coenzyme M reductase operon protein D

Unassigned missing coverage evidence

			seq id	start	end	size	←reads	reads→	gene	description
*	*	÷	NC_003552	836144	836801	658	38 [35]	[34] 36	*MA_RS03755–[MA_RS03760]*	MA_RS03755,[MA_RS03760]
*	*	÷	NC_003552	3204745–3206136	3206136	1–1392	38 [32]	[32] 36	*MA_RS13410–[MA_RS13415]*	MA_RS13410,[MA_RS13415]

fig. S2 Deletion of the *mcrD* gene. (**A**) PCR reactions spanning the *mcrD* gene, as well as primers within the *mcrD* coding sequence were used to verify *mcrD* deletion and rule out wild type contamination. Genomic DNA was used as a template from wildtype (WT; WWM60), initial colony selected from Puromycin plate that contains the gene editing plasmid (Pur), and three colonies from 8-aza-2,6-diaminopurine (8ADP) containing plates used for counterselection against the gene editing plasmid. PCR1 spans the *mcrD* gene, showing a full-sized product only in WT and expected truncated size post gene editing. Similarly, only WT generates a product in PCR 2 and 3 with primers binding within *mcrD*. PCR4 amplifies the *pac* gene conferring puromycin resistance on the gene editing plasmid, verifying plasmid curing by 8ADP counterselection (Nayak and Metcalf 2017). (**B**) Breseq comparison of DDN103 to *M. acetivorans* C2A reference genome. All mutations and missing coverage are identical to the parental strain WWM60 (Nayak and Metcalf 2017) besides the 456 bp deletion of *mcrD* (MA_RS23715). RA: read alignment, MC: missing coverage, JC: new junction.

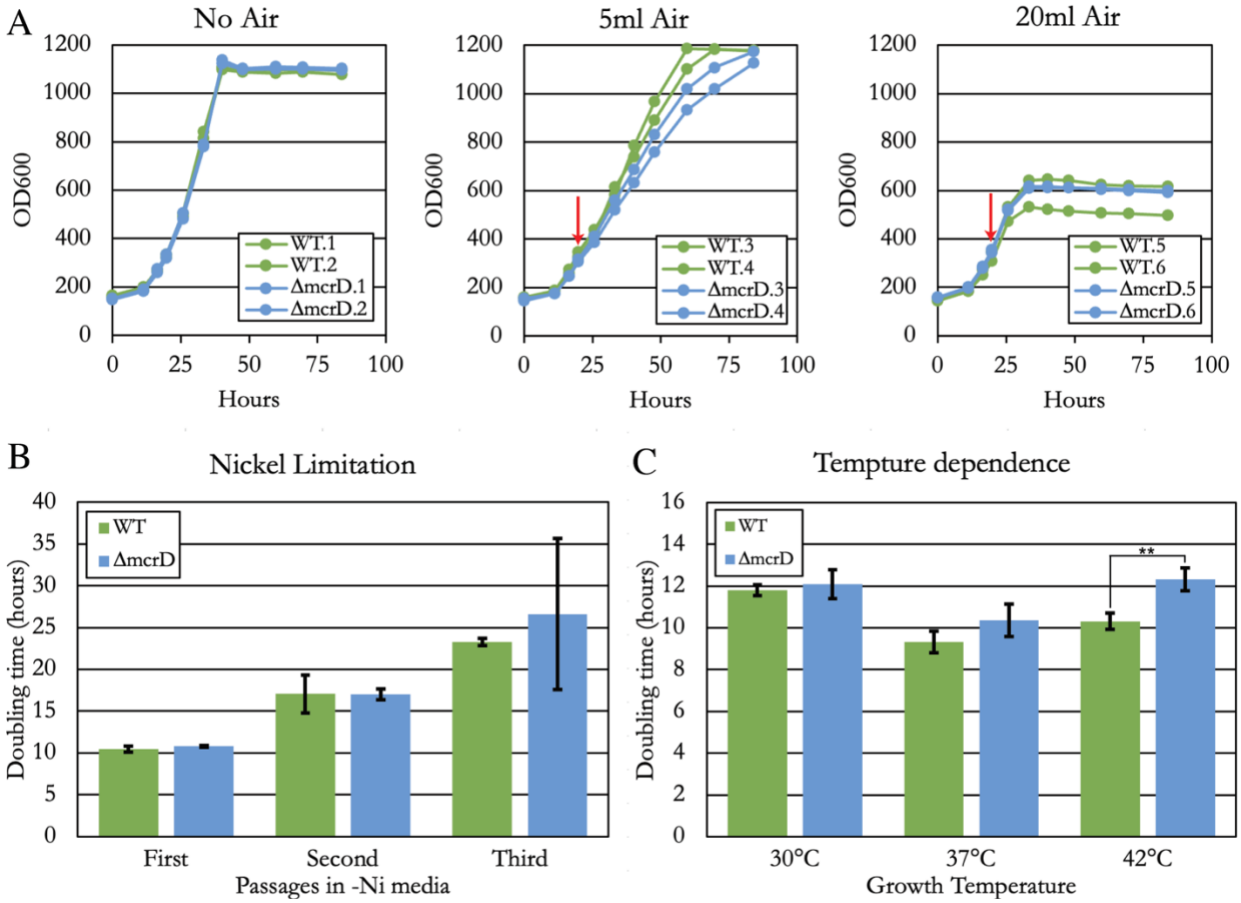

fig. S3 Stress experiments. Attempts to find conditions with a dramatic growth difference between wildtype (WT; WWM60) and Δ*mcrD* were unsuccessful. (**A**) MCR is known to be oxygen sensitive, so air was introduced into growing cultures of WT and Δ*mcrD* at the times indicated by red arrows. Low (5 ml) and high (20 ml) air challenges negatively affected growth, but with no noticeable difference between strains. (**B**) Cultures were washed three times and transferred into methanol media lacking added Ni. Although subsequent passages showed an increase in doubling time for both WT and Δ*mcrD*, no significant difference was observed between strains (two-sided t-test). (**C**) Growth in methanol media in non-ideal low (30°C) and high (42°C) temperatures was assessed. In neither case was the Δ*mcrD* dramatically worse than WT, although at 42°C there was a statistically significant difference (p-value < 0.01, two-sided t-test). Error bars in **B** and **C** represent standard deviations of triplicate cultures.

A

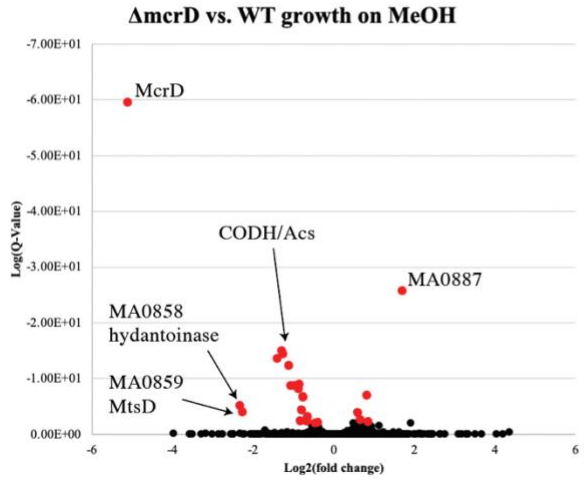

B

Locus Tag	Annotation	Log2 Fold Change	Q-Value
MA4549	McrD	-5.1	2.46E-60
MA0887	phosphate ABC transporter substrate-binding protein	1.7	1.67E-26
MA4399	acetyl-CoA synthase subunit alpha	-1.3	1.04E-15
MA3860	acetyl-CoA synthase subunit alpha	-1.3	3.80E-15
MA4558	MtsH methyltransferase	-1.4	2.34E-14
MA2690	phosphoenolpyruvate carboxylase	-1.1	4.17E-13
MA1012	acetyl-CoA synthase subunit delta	-0.9	1.08E-09
MA3864	acetyl-CoA synthase subunit delta	-0.9	1.08E-09
MA3862	acetyl-CoA synthase subunit beta	-1.0	1.69E-09
MA3861	CO dehydrogenase/acetyl-CoA synthase complex subunit epsilon	-1.1	1.73E-09
MA1014	acetyl-CoA synthase subunit beta	-0.9	6.93E-09
MA4563	hydantoinase/oxoprolinase family protein	0.8	8.87E-08
MA3865	acetyl-CoA synthase subunit gamma	-0.8	1.72E-07
MA1011	acetyl-CoA synthase subunit gamma	-0.8	2.30E-07
MA0858	hydantoinase/oxoprolinase family protein	-2.3	6.05E-06
MA2914	XRE family transcriptional regulator	-0.8	3.79E-05
MA0859	MtsD methyltransferase	-2.3	9.08E-05
MA4384	MtsF methyltransferase	0.6	1.10E-04
MA4649	CBS domain-containing protein	-0.7	6.63E-04
MA4387	hypothetical protein	0.6	0.0020
MA4561	ATPase	-0.8	0.0038
MA1013	ATP-binding protein	-0.7	0.0043
MA3863	ATP-binding protein	-0.7	0.0043
MA3918	ammonium transporter	0.9	0.0051
MA0456	MtaB1 methanol-5-hydroxybenzimidazolylcobamide methyltransferase	-0.4	0.0067
MA0455	MtaC1 methanol-5-hydroxybenzimidazolylcobamide methyltransferase	-0.5	0.0090

fig. S4 Transcriptome comparison of Δ*mcrD* and WT. (**A**) Comparison of significantly differentially expressed genes in Δ*mcrD* and WT grown on methanol. Only 25 genes aside from *mcrD* were differentially expressed between the two strains (defined as a Q-value<0.01 highlighted in red). There is a downregulation of some carbon metabolism genes including multiple isoforms of CODH/Acs and PEP carboxylase, perhaps suggestive of a decrease in carbon flow towards biomass production. All fold changes are relatively minor, at or below two-fold difference. Importantly, other MCR genes are not differentially expressed, revealing that the absence of the *mcrD* gene has not affected the stability of the MCR operon transcript, or resulted in a transcriptional change in this operon. (**B**) Locus tags, annotations log2 fold change and Q-values for all 25 genes.

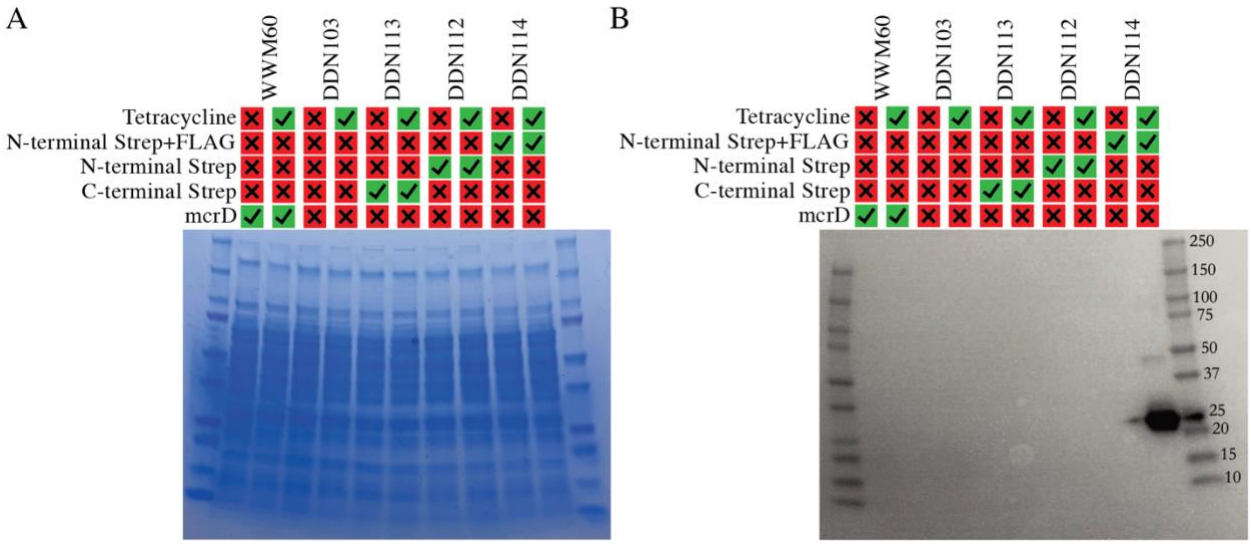

fig. S5 Expression of McrD *in trans*. (A) Coomassie and **(B)** anti-FLAG Western blot of crude protein extracts from *M. acetivorans* strains. Only strain DDN114, which contains a plasmid encoded *mcrD* with a N-terminal twin FLAG and Strep tags showed immunolabelling at the expected size. The plasmid encoded *mcrD* is under the control of a tetracycline-inducible promoter and 100 µg/mL tetracycline was added to the growth medium to induce expression of the tagged McrD protein.

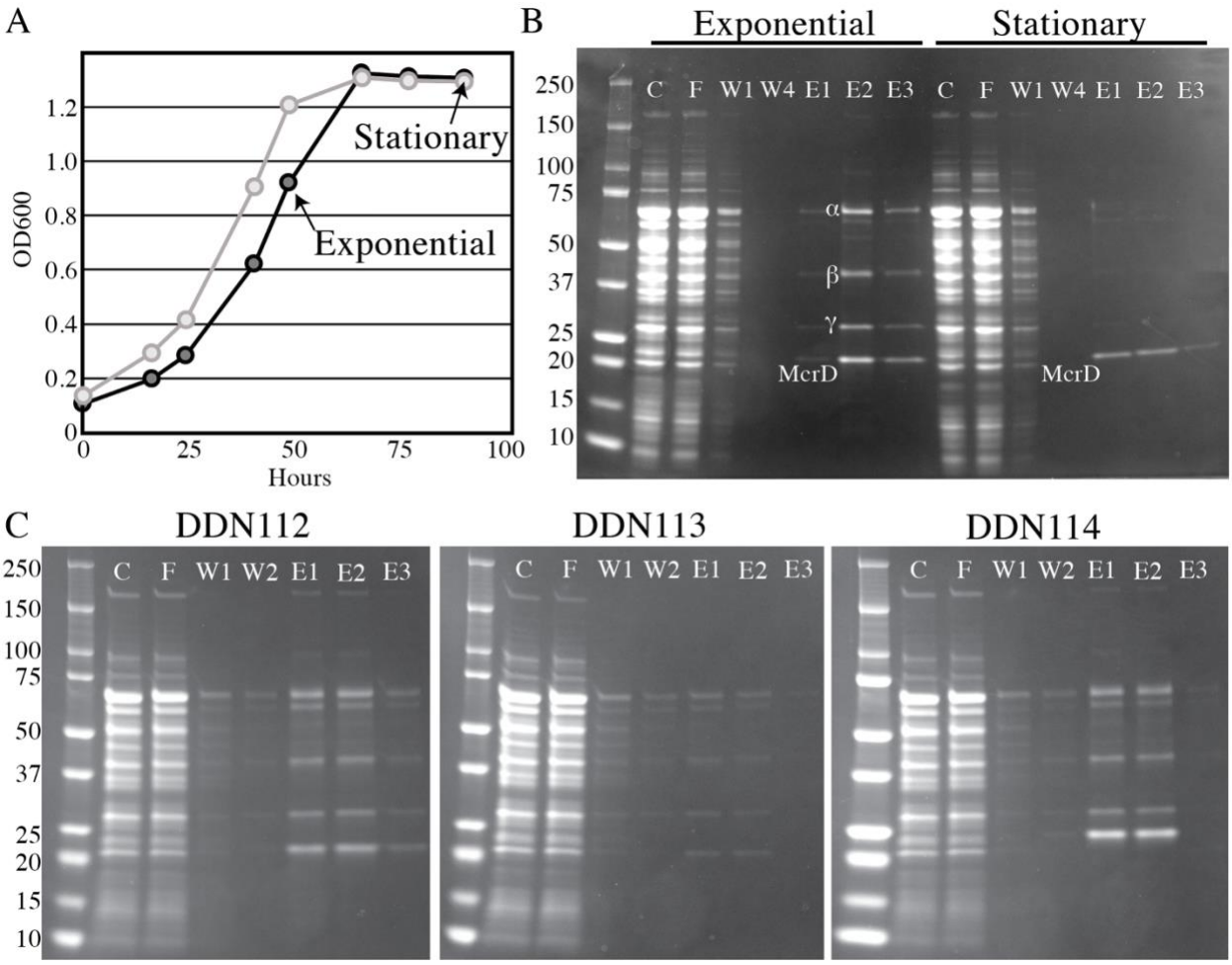

fig. S6 Purification of the McrABGD complex. (**A**) 500 mL cultures of DDN114 were grown and harvested in late exponential (dark gray line) or stationary phase (light gray line) for purification for the McrABGD complex. Optical density readings displayed here were taken from Balch tubes set up in parallel to the large format bottle incubations to determine the growth phase. Arrows indicate the timepoint where the 500mL cultures were harvested. (**B**) SDS-PAGE gels showing Crude cell lysate (C), flow-through of Strep-Tactin Superflow Plus resin used for affinity purification (F), first wash (W1), fourth and final wash (W4), first, second and third elution (E1, E2 and E3, respectively). Protein purification from exponential phase demonstrate roughly stoichiometric amounts of subunits α, β, γ and δ, while cells in stationary phase yield almost entirely δ free from other proteins. **C**) Comparison of tags on the co-purification of MCR subunits. DDN112 (N-terminal Strep only), DDN113 (C-terminal Strep only) and DDN114 (N-terminal FLAG and Strep) all pulled down α, β and γ subunits along with the dominant δ band. Note: the band below the α subunit was identified as Hsp60 (MA0086) but was not detected in the cryoEM data (data not shown).

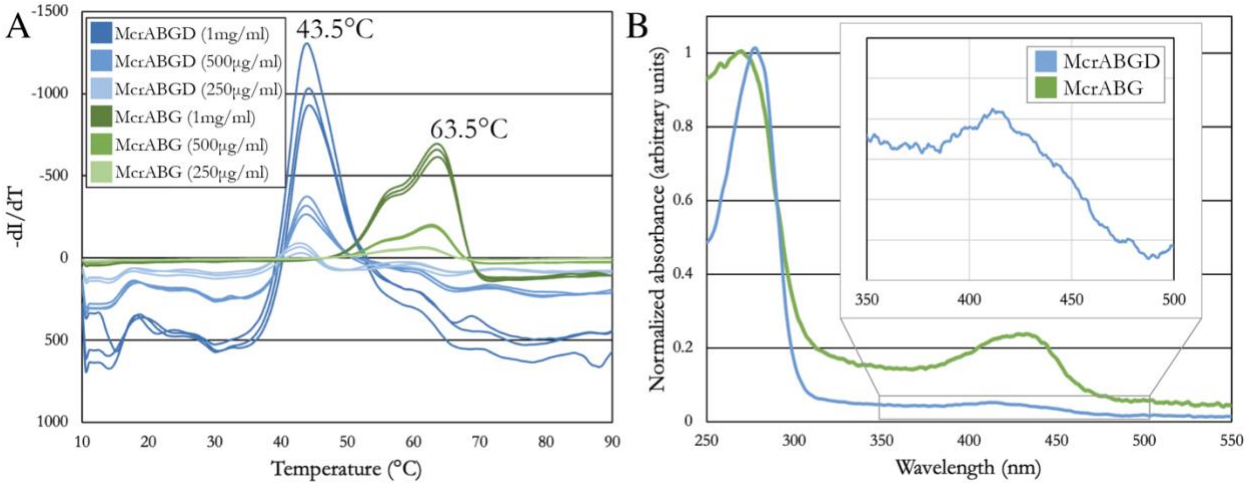

fig. S7 Properties of McrABGD complex. (**A**) SYPRO Orange melt curve analysis of McrABGD complex purified from DDN114 reveals a 20°C lower melting temperature than McrABG purified from WWM1086. (**B**) Absorbance spectra of McrABGD complex purified from DDN114 and McrABG purified from WWM1086. Inset region of showing weak absorbance between 400 and 450 nm consistent with sub-stoichiometric loading of McrABGD complex with cofactor F_{430}.

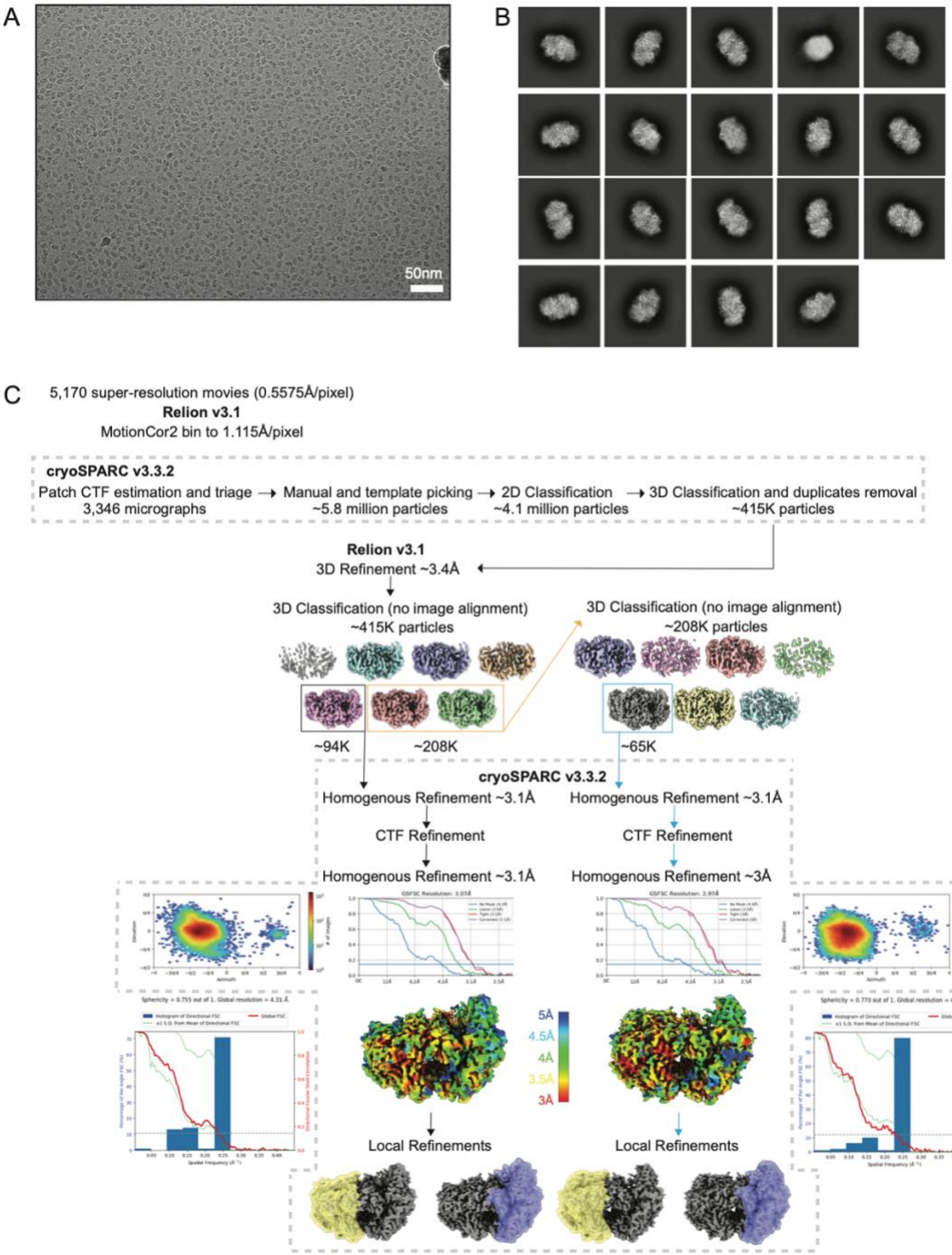

fig. S8 Cryo-EM processing pipeline. (**A**) Example micrograph of the McrABGD complex at -2.1 µm estimated average defocus. Scale bar, 100Å. (**B**) Representative 2D class averages generated in cryoSPARC. The edge of each box corresponds to 250Å. (**C**) EM density from a well-resolved region of the final 3D reconstructions. (**D**) Flow chart depicting the steps taken during data processing to generate the two distinct conformational reconstructions of McrD-bound MCR complex. Steps enclosed in gray dashed boxes were performed in cryoSPARC. Sphericity was calculated using the 3DFSC script from D. Lyumkis, available at https://3dfsc.salk.edu.

412

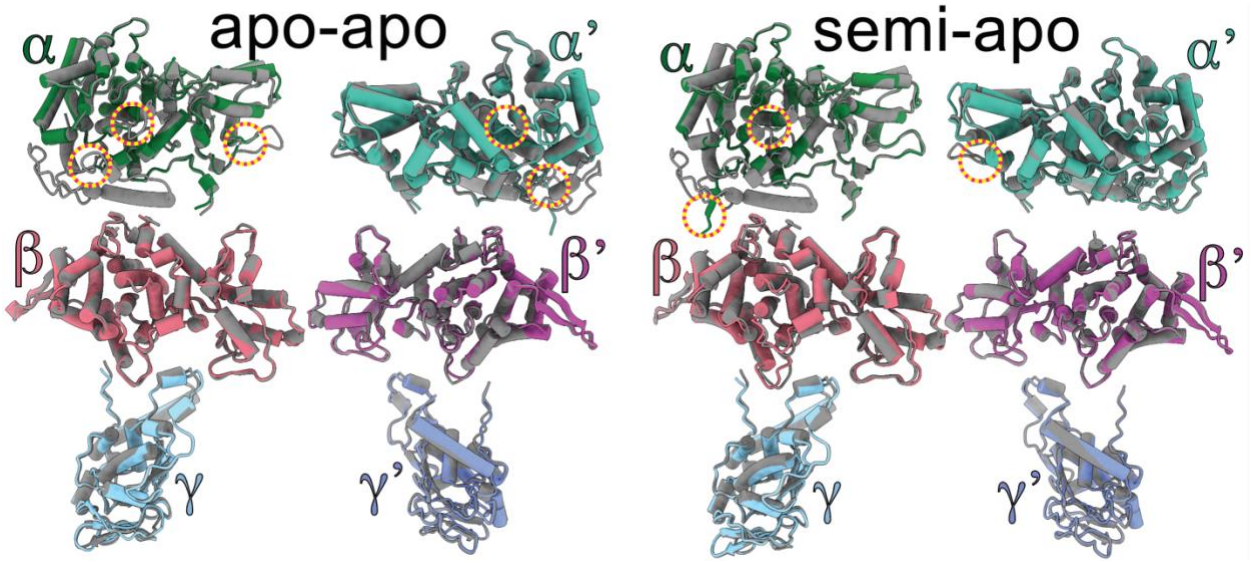

413
414

415 **fig. S9 Details of individual chains.** Each individual subunit of MCR from the cryoEM models
416 reported here are aligned to their corresponding subunit from PDB:1e6y. Overlays highlight the
417 extensive structural similarity, while major differences are highlighted in yellow dashed circles.

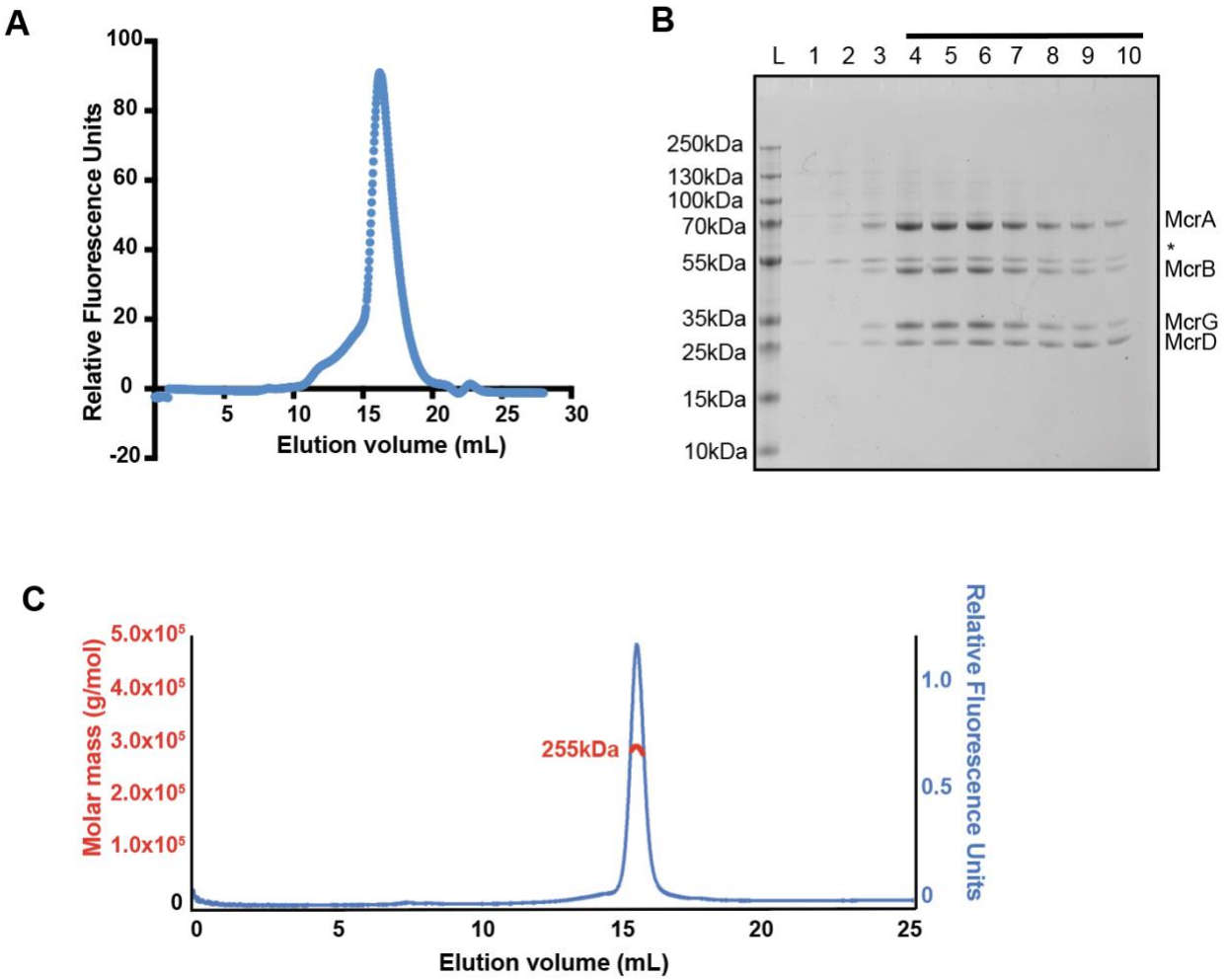

fig. S10 Size of the McrABGD complex and sample preparation for CryoEM. (A) Representative UV trace from gel filtration of the McrABGD complex on a Superose 6 Increase 10/300 GL. (**B**) Coomassie-stained gel corresponding to the peak fractions in **A**, * indicates multimeric McrD complex due to incomplete denaturating conditions in the gel (McrD verified by mass spectrometry, data not shown). (**C**) Representative trace of the purified McrABGD complex after gel filtration from SEC-MALS experiment.

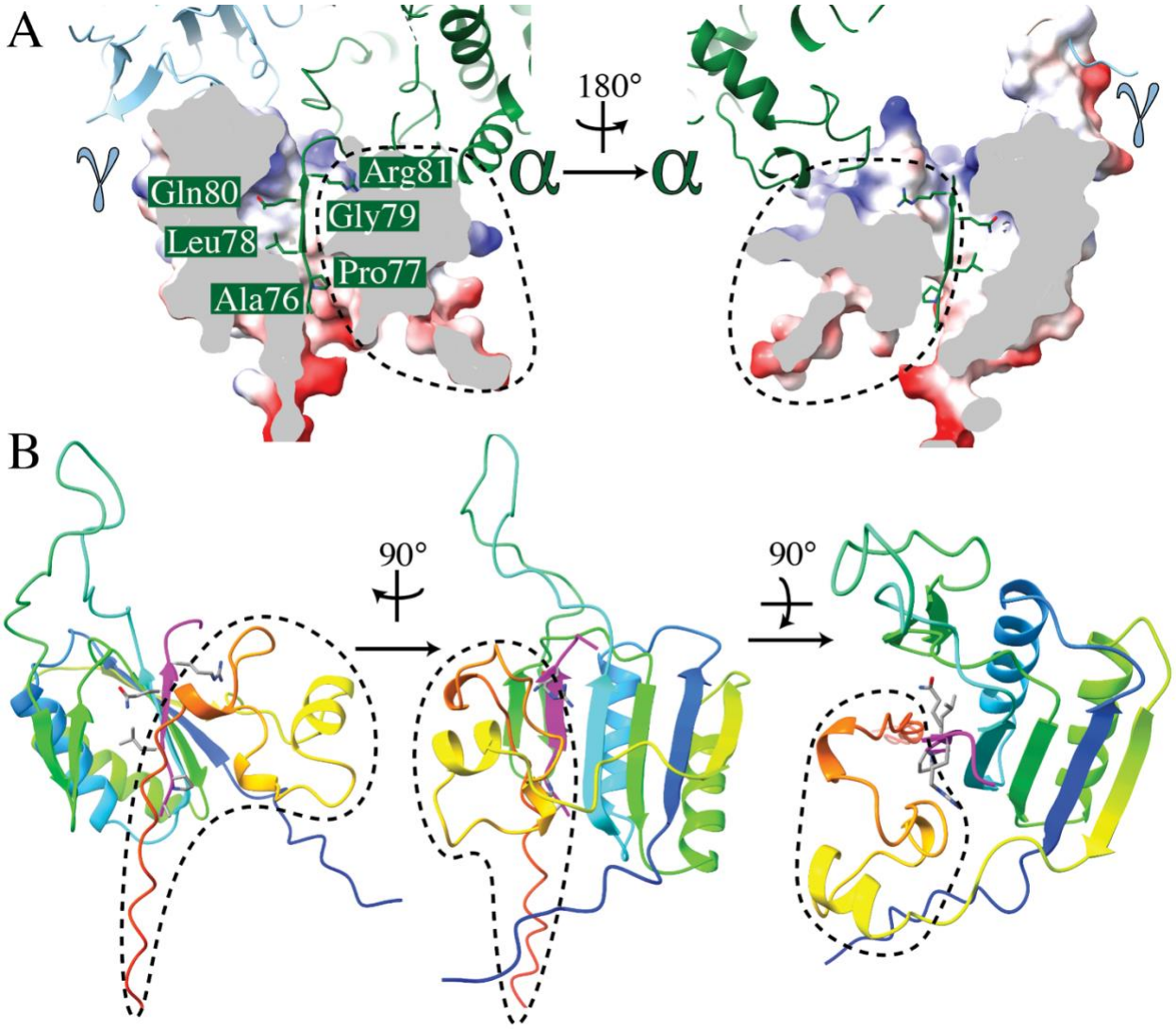

fig. S11 Unresolved C-terminal domain of McrD. The C-terminal domain of McrD past Asp^{D129} does not have corresponding CryoEM density (Tyr ^{D130}-Glu^{D170}). The AlphaFold2 prediction of tagged McrD which matches the N-terminal domain nearly perfectly predicts these C-terminal residues to fold in a way that produces a channel into which the residues Ala$^{\alpha 76}$-Arg$^{\alpha 81}$ fit neatly. (**A**) Two views of this interface with a cartoon diagram of the α and γ subunits and surface cutaway of the AlphaFold2 prediction of McrD. Side chains for Ala$^{\alpha 76}$-Arg$^{\alpha 81}$ are shown to highlight the fit. (**B**) Three views of the same interface with the McrD prediction shown as a cartoon with rainbow coloring. In all panels region of McrD not found in our cryoEM density is outlined with a dashed line.

A

Ion	Calc.	Obs.	Error (ppm)	Ion	Calc.	Obs.	Error (ppm)
$[M+3H]^{3+}$	1144.8552	1144.8502	4.37	$y3^{+}$	417.2456	417.2438	4.31
$b4^{+}$	465.2496	465.2476	4.26	$y4^{+}$	532.2726	532.2700	4.96
$b6^{+}$	685.3167	685.3137	4.35	$y5^{+}$	629.3253	629.3227	4.15
$b8^{+}$	913.4277	913.4243	3.77	$y6^{+}$	742.4094	742.4065	3.92
$b9^{+}$	1041.4863	1041.4821	4.07	$y7^{+}$	799.4308	799.4278	3.75
$b12^{+}$	1399.5810	1399.5752	4.14	$y8^{+}$	928.4734	928.4699	3.76
$b14^{+}$	1527.6396	1527.6348	3.16	$y9^{+}$	1043.5004	1043.4959	4.36
$b15^{+}$	1628.6873	1628.6818	3.40	$y10^{+}$	1100.5218	1100.5173	4.06
$b16^{+}$	1742.7302	1742.7274	1.60	$y11^{+}$	1228.5804	1228.5759	3.64
$b17^{+}$	1841.7986	1841.7903	4.52	$y12^{+}$	1391.6437	1391.6384	3.79
$b18^{+}$	1954.8827	1954.8742	4.37	$y13^{+}$	1478.6758	1478.6707	3.48
$b22^{2+}$	1195.5327	1195.5282	3.76	$y14^{+}$	1591.7598	1591.7539	3.70
$b24^{2+}$	1317.5674	1317.5613	4.64	$y16^{2+}$	902.9392	902.9360	3.50
$b25^{2+}$	1346.0782	1346.0728	4.05	$y17^{2+}$	953.4631	953.4597	3.61
$b26^{2+}$	1402.6202	1402.6146	3.98	$y18^{2+}$	988.9816	988.9787	2.93
$b29^{2+}$	1573.1813	1573.1785	1.80	$y19^{2+}$	1017.4924	1017.4882	4.17
				$y23^{2+}$	1260.5690	1260.5652	3.02
				$y25^{2+}$	1374.6245	1374.6189	4.07

B

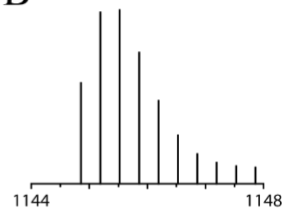

C

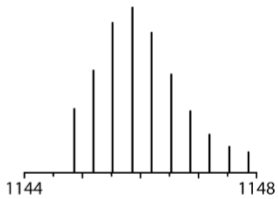

fig. S12 HRMS/MS analysis of an McrA tryptic peptide (Leu^{461}-Arg^{491}, m/z 1144.85). (A) Table of daughter ion assignments for an McrA tryptic peptide confirming three PTMs- thio Gly^{465}, didehydro Asp^{470} and methyl Cys^{472} for fragmentation and annotated CID spectrum shown in Fig. 2D. Calculated isotope distribution for the parent ion **(B)** with thio Gly^{465}, dehydro Asp^{470} and methyl Cys^{472} **(C)** 1:1 mixture of tryptic peptides having or lacking dehydro Asp^{470} and containing thio Gly^{465} and methyl Cys^{472}. The observed isotope distribution of the parent ion in **Fig. 2D** is similar to that in **(C)** suggesting that Asp^{470} is unmodified in some fragments.

A

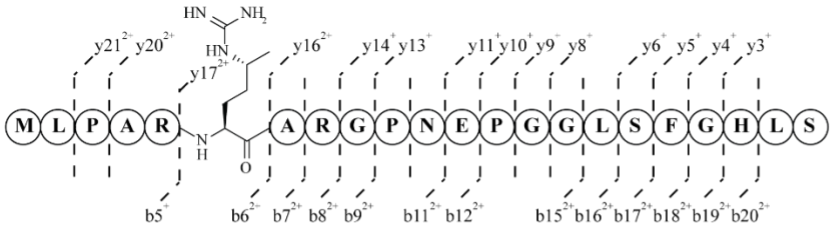

B

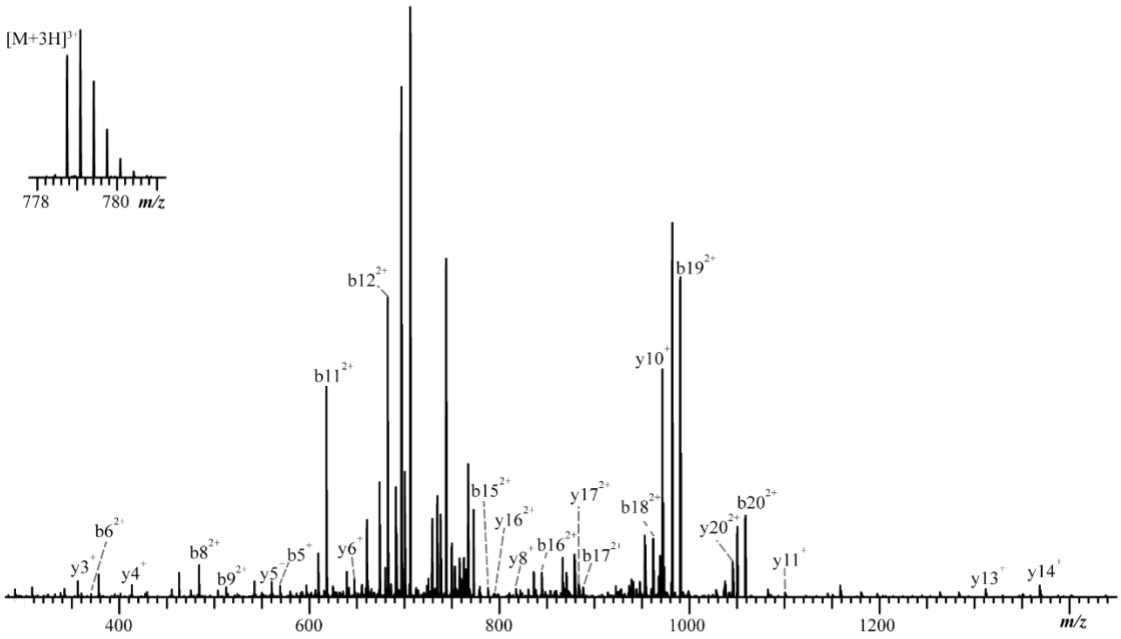

C

Ion	Calc.	Obs.	Error (ppm)
$[M+3H]^{3+}$	778.7464	778.7459	0.68
$b5^{+}$	569.3228	569.3222	1.05
$b6^{2+}$	370.2234	370.2230	1.11
$b7^{2+}$	405.7420	405.7416	1.11
$b8^{2+}$	483.7925	483.7919	1.24
$b9^{2+}$	512.3033	512.3026	1.46
$b11^{2+}$	617.8511	617.8503	1.33
$b12^{2+}$	682.3724	682.3713	1.55
$b15^{2+}$	787.9203	787.9194	1.18
$b16^{2+}$	844.4623	844.4611	1.40
$b17^{2+}$	887.9783	887.9771	1.34
$b18^{2+}$	961.5125	961.5111	1.51
$b19^{2+}$	990.0232	990.0214	1.80
$b20^{2+}$	1058.5527	1058.5508	1.81

Ion	Calc.	Obs.	Error (ppm)
$y3^{+}$	356.1928	356.1924	1.26
$y4^{+}$	413.2143	413.2138	1.33
$y5^{+}$	560.2827	560.2820	1.29
$y6^{+}$	647.3148	647.3138	1.48
$y8^{+}$	817.4203	817.4192	1.36
$y9^{+}$	874.4417	874.4409	0.96
$y10^{+}$	971.4945	971.4929	1.63
$y11^{+}$	1100.5371	1100.5344	2.44
$y13^{+}$	1311.6328	1311.6306	1.66
$y14^{+}$	1368.6543	1368.6521	1.61
$y16^{2+}$	798.3999	798.3989	1.30
$y17^{2+}$	883.4583	883.4570	1.51
$y20^{2+}$	1045.5538	1045.5523	1.48
$y21^{2+}$	1102.0958	1102.0939	1.75

fig. S13 HRMS/MS analysis of an McrA AspN-GluC double-digest peptide (Met^{280}-Ser^{301}, m/z 778.74). (A) Fragmentation **(B)** Annotated CID spectrum of an McrA AspN-GluC double-digest peptide confirming methyl Arg^{285}. Observed b and y ions are annotated. **(C)** Table of daughter ion assignments.

A

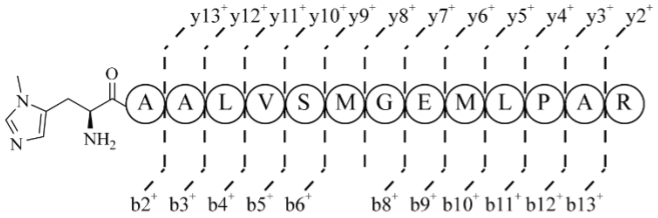

B

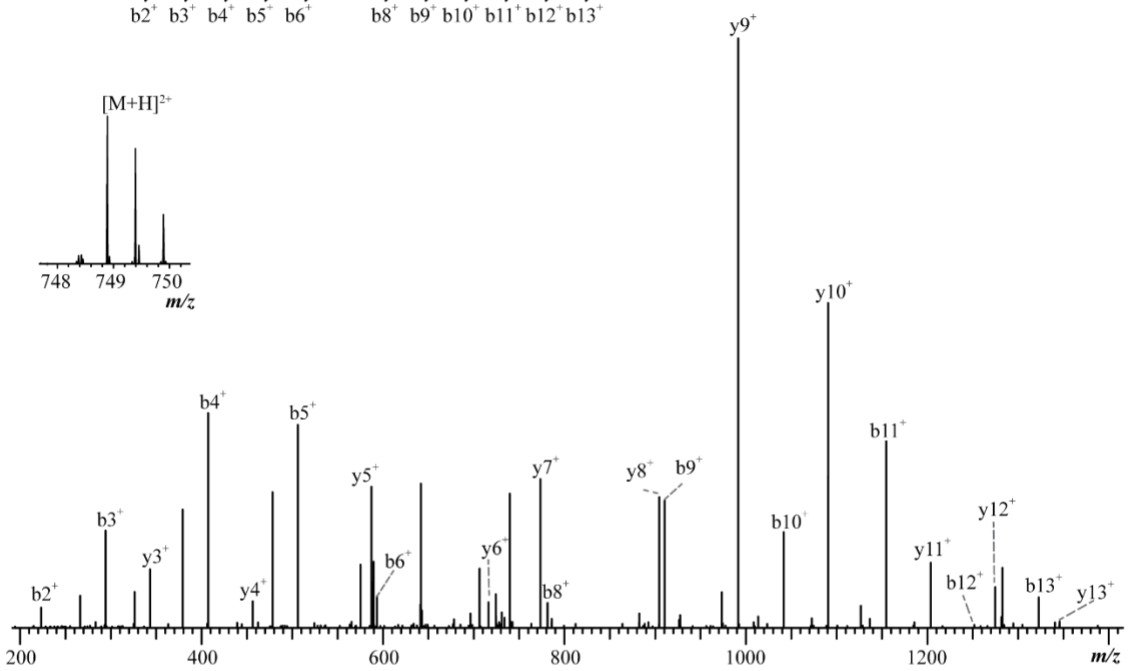

C

Ion	Calc.	Obs.	Error (ppm)
[M+H]$^+$	748.8892	748.8900	-1.02
b2$^+$	223.1190	223.1191	-0.45
b3$^+$	294.1561	294.1563	-0.68
b4$^+$	407.2402	407.2405	-0.74
b5$^+$	506.3086	506.3090	-0.79
b6$^+$	593.3406	593.3412	-1.01
b8$^+$	781.4026	781.4036	-1.28
b9$^+$	910.4452	910.4462	-1.10
b10$^+$	1041.4856	1041.4865	-0.86
b11$^+$	1154.5697	1154.5703	-0.52
b12$^+$	1251.6225	1251.6228	-0.24
b13$^+$	1322.6596	1322.6608	-0.91

Ion	Calc.	Obs.	Error (ppm)
y2$^+$	246.1561	246.1562	-0.41
y3$^+$	343.2088	343.2091	-0.87
y4$^+$	456.2929	456.2933	-0.94
y5$^+$	587.3334	587.3340	-1.02
y6$^+$	716.3760	716.3767	-0.98
y7$^+$	773.3974	773.3984	-1.29
y8$^+$	904.4379	904.4388	-1.00
y9$^+$	991.4699	991.4707	-0.81
y10$^+$	1090.5384	1090.5389	-0.46
y11$^+$	1203.6224	1203.6232	-0.66
y12$^+$	1274.6595	1274.6608	-1.02
y13$^+$	1345.6967	1345.6982	-1.11

fig. S14 HRMS/MS analysis of an McrA tryptic peptide (His^{271}-Arg^{285}, m/z 748.88). (A) Fragmentation **(B)** Annotated CID spectrum of an McrA tryptic peptide confirming *N*-methyl His^{271}. Observed b and y ions are annotated. **(C)** Table of daughter ion assignments.

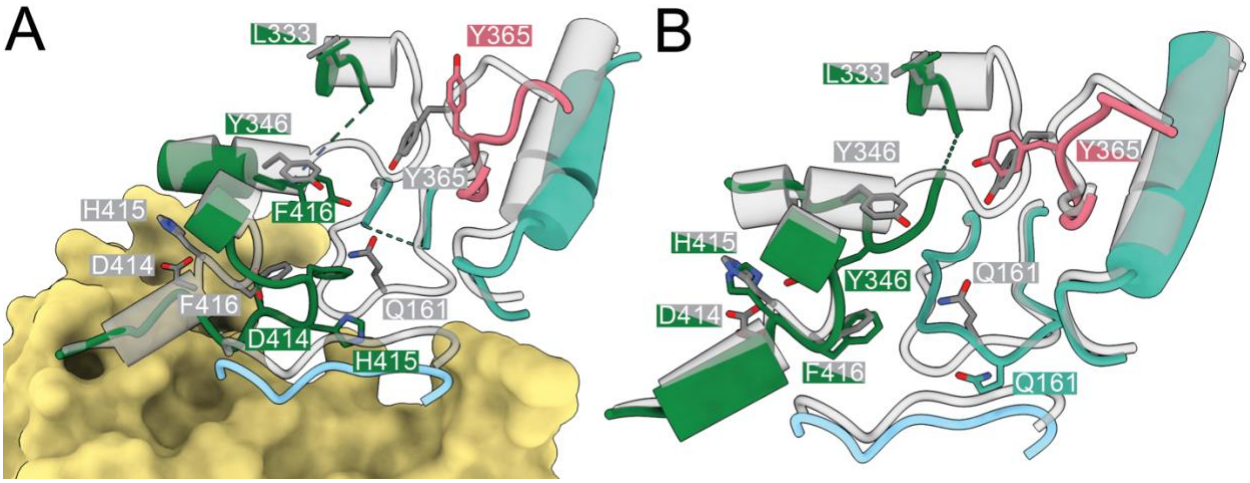

fig. S15 Active site details of apo-apo model. (**A**) McrD-bound active site in the apo-apo model shows similar deformations compared to that in the semi-apo model (**Fig. 3D**). (**B**) The contralateral active site in the apo-apo model shows a unique conformation, with notable displacements to the F_{430} axial ligand $Q^{\alpha'161}$ and a partially resolved disordered loop between $Y^{\alpha346}$ and $L^{\alpha333}$.

469 **Supplementary Table 1**: List of primers used in this study
470

Name	Description	Primer Sequence (Overhangs for Gibson assembly are shown in red)
VI095	Fwd primer pac region for colony PCR. Product size 1061bp	CTCCATTCATGGGGTCGTGC
VI096	Rev primer pac region for colony PCR. Product size 1061bp	GGAACTTCTGATATCGAATTCATCGC
GLC053	Rev primer for adding McrD guide	ATTCAGATCGGAGATCAGGTACATGTG CTTACAGC
GLC054	Fwd primer for adding McrD guide	ACCTGATCTCCGATCTGAATGTTTTAGA GCTAGAAATAGC
GLC060	Fwd primer for McrD KO repair template fragment 1	GCCTTTTTTTTTCGAAGTTTAACCACAG TTGGTGCAGCA
GLC061	Rev primer for McrD KO repair template fragment 1	TGTCATCTTCATCTTCCGTGTTTGAAGC AGAG
GLC062	Fwd primer for McrD KO repair template fragment 2	CACGGAAGATGAAGATGACACTGATAA AGATGAGTGA
GLC063	Rev primer for McrD KO repair template fragment 2	GATGTTGTTCCTGCAGGTTTTACACCTC TGAAGTTGATTGCTG
GLC073	Fwd sequencing primer for *mcrD* KO	AAGACGGTGTAATCTCC
GLC074	Rev sequencing primer for *mcrD* KO	TTCAACAATCTGACGGC
GLC075	Fwd primer for amplifying McrD for gibson assembly into pJK027A	AATAAATTAAGGAGGAAATTCAATGTC AGACTCTGCTTCAAACAC
GLC076	Rev primer for amplifying McrD for gibson assembly into pJK027A	CATTATACGAAGTTATCAAGATCACTCA TCTTTATCAGTGTCA
GLC077	Rev primer for amplifying McrD-C-strep for gibson assembly into pJK027A	CATTATACGAAGTTATCAAGATCATTTT TCAAACTGAGGATGTGACC
GLC078	Rev primer for amplifying McrD-C-strep-flag for gibson assembly into pJK027A	CATTATACGAAGTTATCAAGATCACTTG TCGTCATCGTCTTTG
GLC079	Fwd primer for amplifying McrD-strep for gibson assembly into pJK027A	AATAAATTAAGGAGGAAATTCAATGTG GTCACATCCTCAGTTTGA
GLC080	Fwd primer for amplifying McrD-flag-strep for gibson assembly into pJK027A	AATAAATTAAGGAGGAAATTCAATGGA CTACAAAGACGATGACGA
GLC081	Rev primer to add strep and linker to c-terminus of McrD	TCATTTTTCAAACTGAGGATGTGACCA TCCTCCACCCTCATCTTTATCAGTGT
GLC082	Rev primer to add flag and linker to c-terminus of McrD-strep	TCACTTGTCGTCATCGTCTTTGTAGTCA CCGCCTCCTTTTTCAAACTGAGGATG
GLC083	Fwd primer to add strep and linker to n-terminus of McrD	ATGTGGTCACATCCTCAGTTTGAAAAA GGAGGCGGTATGTCAGACTCTGCTTC

GLC084	Rev primer to add flag and linker to n-terminus of McrD-strep	ATGGACTACAAAGACGATGACGACAAG GGTGGAGGATGGTCACATCCTCAGTT
GLC091	Fwd primer to amplify from within *mcrD*	TTCCTCAGAAGAAAGCC
GLC092	Rev primer to amplify from within *mcrD*	TTTTCGATTTCAAGCCTG

471
472

Supplementary Table 2: List of plasmids used in this study

Plasmid	Features	Source
pAMG40	Vector for fosmid retrofitting that contains pC2A and λattB	(Guss *et al.* 2008)
pJK027A	Vector with P*mcrB*(*tetO1*) promoter fusion to *uidA* that contains φC31-attB and λattP	(Guss *et al.* 2008)
pDN201	pJK027A-derived plasmid with P*mcrB*(*tetO1*) promoter fusion to Spy *cas9*	(Nayak and Metcalf, 2017)
pGLC009	pDN201-derived plasmid with synthetic fragments containing PmtaCB1 promoter fusion to sgRNA targeting the *mcrD (MA4549)* CDS	This study
pGLC011	pGLC009-derived plasmid containing a repair template to generate an in-frame deletion of the *mcrD (MA4549)* CDS	This study
pGLC013	Cointegrate of pGLC011 and pAMG40	This study
pGLC023	pJK027A-derived plasmid with P*mcrB*(*tetO1*) promoter fusion to *mcrD (MA4549)* CDS from *M. acetivorans*	This study
pGLC024	pJK027A-derived plasmid with P*mcrB*(*tetO1*) promoter fusion to *mcrD (MA4549)* CDS from *M. acetivorans* with a C-terminal Strep tag	This study
pGLC026	pJK027A-derived plasmid with P*mcrB*(*tetO1*) promoter fusion to *mcrD (MA4549)* CDS from *M. acetivorans* with a N-terminal Strep tag	This study
pGLC027	pJK027A-derived plasmid with P*mcrB*(*tetO1*) promoter fusion to *mcrD (MA4549)* CDS from *M. acetivorans* with a N-terminal tandem Strep and FLAG tags	This study
pGLC028	Cointegrate of pGLC023 and pAMG40	This study
pGLC029	Cointegrate of pGLC024 and pAMG40	This study
pGLC031	Cointegrate of pGLC026 and pAMG40	This study
pGLC032	Cointegrate of pGLC027 and pAMG40	This study

Supplementary Table 3: List of *Methanosarcina acetivorans* strains used in this study

Strain	Genotype	Source
WWM60	Δ*hpt*::P*mcrB-tet*R	(Guss *et al.*, 2008)
WWM1086	Δ*hpt*::*PmcrB-tetR,* Enterokinase cleavable TAP-tag at N-terminus of *mcrG*	(Nayak *et al.*, 2020)
DDN103	Δ*hpt*::P*mcrB-tetR,* Δ*mcrD*	This study
DDN111	DDN103/pGLC028 [*PmcrB(tetO1)-mcrD*]	This study
DDN112	DN103/pGLC029 [*PmcrB(tetO1)-mcrD*-C-terminal strep tag]	This study
DDN113	DN103/pGLC031 [*PmcrB(tetO1)*- N-terminal strep tag-*mcrD*]	This study
DDN114	DN103/pGLC032 [*PmcrB(tetO1)*- N-terminal strep and FLAG tag -*mcrD*]	This study

Supplementary Table 4: CryoEM structure statistics reported in this study

	Semi-apo (EMDB: XXXX) (PDB:XXXX)		Apo-apo (EMDB: XXXX) (PDB:XXXX)	
	Composition (#)			
Chains	10		7	
Atoms	19180		18317	
Protein residues	2515		2422	
Ligands	F43, TP7, CoM		---	
	Bonds (RMSD)			
Length (Å) (# > 4σ)	0.007 (2)		0.010 (1)	
Angles (°) (# > 4σ)	1.108 (7)		1.376 (16)	
MolProbity score	2.27		1.88	
Clash score	28.08		10.76	
	Ramachandran plot (%)			
Outliers	0.0		0.0	
Allowed	4.77		4.75	
Favored	95.23		95.25	
	Rama-Z (Ramachandran plot Z-score, RMSD)			
whole (N=2475)	0.25 (0.17)		2.31 (0.15)	
helix (N=1209)	0.57 (0.15)		1.42 (0.13)	
sheet (N=140)	0.54 (0.48)		1.50 (0.42)	
loop (N=1126)	0.89 (0.18)		1.53 (0.17)	
Rotamer outliers (%)	0.10		0.26	
Cβ outliers (%)	0.09		0.05	
	Peptide plane (%)			
Cis proline/general	2.0/0.0		2.1/0.0	
Twisted proline/general	0.0/0.0		0.0/0.0	
CaBLAM outliers (%)	2.14		2.94	
	ADP (B-factors)			
Iso/Aniso (#)	19129/0		18317/0	
Protein (min/max/mean)	30.00/122.52/62.31		30.00/151.67/82.67	
Ligand (min/max/mean)	55.70/59.00/58.08		---	
	Occupancy			
Mean	1.00		1.00	
occ = 1 (%)	100.00		100.00	
occ > 1 (%)	0.00		0.00	
	Resolution estimates (Å)			
	Masked	Unmasked	Masked	Unmasked
d FSC (half maps; 0.143)	3.2	3.4	3.2	3.5
d 99 (full/half1/half2)	3.7/2.3/2.3	3.6/2.3/2.3	3.9/2.3/2.3	3.8/2.3/2.3
d model	3.4	3.4	3.5	3.5
d FSC model (0/0.143/0.5)	2.9/3.0/3.3	2.9/3.0/3.5	3.0/3.1/3.5	3.0/3.1/3.7
Map min/max/mean	-0.78/1.70/0		-0.64/1.71/0	
	Model vs. Data			
CC (mask)	0.84		0.80	
CC (box)	0.87		0.87	
CC (peaks)	0.82		0.78	
CC (volume)	0.84		0.80	
Mean CC for ligands	0.81		---	

Supplementary Methods

sgRNA design and plasmid construction

The Cas9 single guide RNA (sgRNA) sequence used in this study for genome editing was ACCTGATCTCCGATCTGAAT**AGG** (PAM sequence bold and underlined) and was generated with Geneious Prime v. 11.0. This guide targets the *mcrD* gene (MA4549) and matches 5,600,053-5,600,075 (+strand) in the *M. acetivorans* C2A genome. The CRISPR site finder tool was used with an NGG PAM site at the 3' end with no off-target matches to the *M. acetivorans* genome allowed. The plasmids and primers used in this study are listed in Supplementary Tables 1 and 2 and were generated as previously described (*1*).

Growth media and mutant generation

M. acetivorans strains were routinely maintained in 10ml of high salt (HS) media with either acetate (40mM), methanol (125mM) or trimethylamine (50mM) as the sole carbon and energy source as previously described (*2*). For transformation, 10ml cultures in late exponential phase were anaerobically pelleted and subjected to liposome-mediated transformation using establish protocols (*3*). Selection for transformants was carried out on HS media with 50 mM trimethylamine as the carbon source solidified with 1.5% agar and puromycin at 2µg/ml for positive selection. Colonies were screened for the desired mutation (see below) and restruck on plates with 20µg/ml 8ADP for counter selection to remove the genome editing plasmid and generate the clean deletion strain. Strains carrying tetracycline-inducible *mcrD* variants are permanently maintained in 2µg/ml puromycin to retain the expression plasmid. *M. acetivorans* strains used and generated in this study are listed in Supplementary Table 3.

Mutant validation

PCR screening of colonies was carried out on whole cells resuspended in nanopure water amplified with GoTaq® Green Master Mix (Promega Corporation). Primers were designed to amplify across the McrD gene (GLC073/74) and from within the McrD gene (GLC073/92 and GLC074/91). Positive identification of Δ*mcrD* genotype with no wild type contamination came from the expected decrease in product size with the 73/74 primer pair, and no product with the 73/92 or 74/91 primer pairs. PCR primers amplifying the Pac gene (VI095/96) were used to validate the loss of genome editing plasmids by 8ADP counter selection, or the presence of heterologous expression plasmids. Whole genome resequencing of the Δ*mcrD* strain was carried out by extracting genomic DNA from 10ml of stationary phase cuture grown in HS media with trimethylamine using the Qiagen blood and tissue kit (Qiagen, Hilden, Germany). Illumina library preparation and sequencing was carried out at SeqCenter (Pittsburgh, PA). Comparison of the Δ*mcrD* strain to *M. acetivorans* C2A was carried out using the breseq software package (*4*). Raw reads are deposited in the Sequencing Reads Archive (SRA) and are available under the BioProject XXXXXXXX.

Growth measurements

M. acetivorans doubling times were determined by measuring the optical density at 600nm of cultures grown in Balch tubes containing 10ml HS media with growth substrates and media additions as indicated. Measurements were made using a UV-Vis spectrophotometer (Gensys 50, Thermo Fisher Scientific, Waltham, MA). Doubling times were determined by fitting all points in for which the best fit line of the log2 transformed optical density data had >0.99 R^2 values. For

Ni limitation experiments, trace metal solutions were prepared without Ni addition. For oxygen exposure experiments, the indicated volume of lab air was added through a 0.2 µm syringe filter (CellTreat Scientific Products, Pepperall, MA).

RNA extraction and bioinformatic analysis of transcriptome

WWM60 and DDN103 were grown in triplicate in methanol media at 37°C until late log phase (~0.6 OD600). Two ml of culture was sampled and added immediately to equal amounts 37°C Trizol solution (Life Technologies, Carlsbad, CA, USA). After a 5 minute incubation at room temperature 4 ml of ethanol was added to the culture and Trizol mixture. Solution was applied to a Qiagen RNeasy Mini Kit (Qiagen, Hilden, Germany) and extraction proceeded according to the manufacturer's instructions. DNAse treatment, rRNA depletion and Illumina library preparation and sequencing was carried out at SeqCenter (Pittsburgh, PA). Analysis of transcriptome data was carried out on the KBase bioinformatics platform (*5*). Briefly, raw reads were mapped to the *M. acetivorans* C2A genome using Bowtie2 (*6*), assembled using Cufflinks (*7*), and fold changes and significances values were calculated with DESeq2(*8*). Raw reads are deposited in the Sequencing Reads Archive (SRA) and are available under the BioProject XXXXXXXX.

Protein extraction and affinity purification.

For protein purification 500ml cultures of *M. acetivorans* strains were grown in HS media with trimethylamine (100mM). Cells were lysed and cell debris removed as previously described (*9*), with the one modification that the 50mM sodium phosphate was replaced with 50mM Tris HCl (pH 7.0) in all buffers. Strep-tagged proteins were purified using Strep-Tactin Superflow plus resin (Qiagen, Hilden, Germany) as described previously (*9*) again with the sole modification that sodium phosphate buffer was replaced with Tris HCl. Strep-tagged protein complexes were eluted with washing buffer containing 2.5 mM desthiobiotin.

Protein gels

Protein preparations were mixed with 4x Laemmli sample buffer (Bio-Rad, Hercules, CA) and final concentration of 355mM 2-mercaptoethanol and heated at 90°C for 5 minutes before being run on Mini-Protean TGX denaturing SDS-PAGE gel (Bio-Rad, Hercules, CA). Coommassie staining was carried out with GelCode™ Blue Safe Protein Stain (Thermo Fisher Scientific). For immunoblotting, gels were transblotted using the Trans-Blot Turbo transfer system (Bio-Rad, Hercules, CA) onto 0.2 µm PVDF membrane (Bio-Rad, Hercules, CA). Monoclonal anti-Flag M2-Peroxidase (HRP) antibody (Sigma-Aldrich, St Louis, MO) was used at 50,000 fold dilution as previously described (*1*). Immobilon Western Chemiluminescent HRP Substrate (Millipore, Burlington, MA) was used with manufacturer's protocol for detecting HRP-conjugated antibodies. Coomassie and immublots were imaged with the ChemiDoc MP Imaging System (Bio-Rad, Hercules, CA).

Proteolytic digestion of purified McrABDG complex

For in-solution trypsinolysis ($His^{\alpha 271}$-$Arg^{\alpha 285}$, m/z 748.88), 50 µg of purified McrABDG complex was digested with Sequencing Grade Modified Trypsin (1:100 w/w ratio; Promega) at a final McrABDG concentration of 0.5 mg/mL in 50 mM Tris-HCl, 1 mM $CaCl_2$ at 37°C for 14 h. For in-gel trypsinolysis of McrA ($Leu^{\alpha 461}$-$Arg^{\alpha 491}$, m/z 1144.85), 100 µg of purified McrABDG complex was separated by SDS-PAGE. In-gel trypsin digest was performed per established protocols on excised gel pieces corresponding to McrA (*10*).

For AspN and GluC double digestion ($Met^{\alpha 280}$-$Ser^{\alpha 301}$, m/z 778.74), 300 µg of purified McrABDG was digested with endoproteinase GluC (1:200 w/w ratio; Promega) and endoproteinase AspN (1:125 w/w ratio; Promega) at a final McrABDG concentration of 2 mg/mL in 50 mM NH_4HCO_3 pH 8 at 37°C for 14 h. MeCN was added to the resultant digest to a final ratio of 50/50 50 mM aq. NH_4HCO_3/MeCN and centrifuged at 17,000g to remove precipitate. The supernatant was dried using a SpeedVac concentrator prior to purification by HPLC using a Thermo Fisher Vanquish UHPLC equipped with a Thermo Scientific Accucore C18 column (150 × 4.6 mm, 2.6 µm particle size, 80 Å pore size). The dried sample was resuspended in 5/95 10 mM aq. NH_4HCO_3/MeCN and injected with a mobile phase of 10 mM aq. NH_4HCO_3/MeCN and separated using a gradient from 5-65% MeCN over 25 min at 1.5 mL/min. Fractions collected every min were analyzed by MALDI MS to identify those containing peptide fragment of interest. Desired fractions were dried using a SpeedVac concentration for subsequent HRMS/MS analysis.

HRMS/MS analysis of McrA peptide fragments

HPLC-purified, dried samples were resuspended in ESI mix [80% MeCN, 19% H2O, 1% acetic acid]. Digests were desalted using ZipTips, eluted into 75% aq. MeCN, and diluted 1:1 in ESI mix before HRMS/MS analysis. Samples were directly infused onto a ThermoFisher Scientific Orbitrap Fusion ESI-MS using an Advion TriVersa Nanomate 100. MS calibration was performed with Pierce LTQ Velos ESI Positive Ion Calibration Solution (ThermoFisher). The MS was operated using the following parameters: 120,000 resolution, 0.4-2 m/z isolation width (MS/MS), 35 normalized collision energy (MS/MS), 0.4 activation q value (MS/MS), and 30 ms activation time (MS/MS). Fragmentation was performed using collision-induced dissociation (CID) at 30%, 50%, and 70%. Data analysis was conducted using the Qualbrowser application of Xcalibur software (ThermoFisher Scientific).

SEC MALS

A Superose6 10/300 Increase column (Cytiva) was attached in line to an Agilent Technologies 1100 series with a 1260 Infinity lamp, Dawn Heleos II and the Optilab T-Rex (Wyatt Technology) operating on Astra v5.3 software (Wyatt Technology). The system was equilibrated overnight in 25mM Tris pH 8, 150 mM NaCl before standardization with 2mg/mL bovine serum albumin. 125uL of McrABGD sample was injected onto the system at 0.35mL/min and light scattering was used to determine the molecular weight.

Sample preparation for cryoEM

Frozen aliquots of protein were thawed and centrifuged at 21,000g for 5 minutes before gel filtration chromatography on an Akta Purifier (GE) equipped with a Superose6 10/300 Increase column (Cytiva) into GF buffer (25mM Tris pH 8, 150mM NaCl). The peak fractions (see Supplemental Figure) were collected and concentrated in a 100K MWCO spin concentrator (Millipore). 3uL of sample at 0.55mg/mL was deposited onto freshly glow-discharged Quantifoil R 2/1 Copper 300 mesh grids (Electron Microscopy Sciences, CAT# Q310CR1) for 5 seconds before being blotted at 4°C under 100% humidity for 3 seconds in a Vitrobot Mark IV (ThermoFisher) at blot force 18 and plunged into liquid ethane. The grids were glow discharged beforehand for 30s at 25mA at 0.37mBar in a PelCo EasiGlo (Ted Pella, Inc.)

CryoEM data collection

~5,200 super-resolution dose-fractionated images were collected with a total dose of 50^{e-} over a defocus range of -0.8um to -2.0um on a Talos Arctica, equipped with a Gatan K3 camera, operating at 200kV with a nominal magnification of 36,000X and a pixel size of 0.5575Å/pixel. Using SerialEM (*11*), movies were collected in a 9-hole image shift pattern with 2 exposures captured per hole, for a total of 18 images per stage shift.

CryoEM data processing

Movies were motion-corrected with 2x binning using MotionCor2 (*12*) via the RELION wrapper (*13*) and then imported into cryoSPARC (*14*) for patch CTF estimation, micrograph curation, and particle picking, which generated 5.7 million particles. Junk particles were filtered out via 2D Classification, yielding 4.1 million particles. Duplicate particles were removed, and the remaining particles were pruned via 3D classification, by retaining only the classes with obvious density for McrD, leaving 415K particles. This particle set was transferred into RELION via csparc2star.py (*15*), for 3D refinement to generate a consensus reconstruction followed by 3D classification without alignments. Two distinct classes emerged, one with 94K particles and another with 208K particles. The 208K particle stack went through a second round of 3D classification and ultimately yielded a stack with 65K particles. The separate 94K and 65K particle stacks were imported back into cryoSPARC for additional homogenous refinements, CTF refinement, and estimation of local resolution. 3DFSC (*16*) was used to measure the directional resolution anisotropy. Due to high anisotropy and variability in resolution, local refinements were performed using masks at each end of the molecule. The local refinement maps were combined into composite maps using Phenix (*17*). A mix of composite, sharpened, and local refinement maps was used for interpretation.

Model building and refinement

A crystal structure of McrABG complex (pdb: 1e6y) was docked into the semi-apo map but left a sizeable patch of density unoccupied (*18*). An AlphaFold2 prediction of McrD was simultaneously placed into the remaining density (*19*), and together these models were used as the starting point for manual rebuilding throughout the cryoEM density using Coot (*20*). The resulting semi-apo model was docked into the apo-apo map and used as the initial model for manual rebuilding. The rebuilt models were iteratively refined in real space using Phenix, and figures were produced using ChimeraX (*21*).

1. D. Gupta, K. E. Shalvarjian, D. D. Nayak, An Archaea-specific c-type cytochrome maturation machinery is crucial for methanogenesis in Methanosarcina acetivorans. *eLife*. **11**, e76970 (2022).

2. K. R. Sowers, J. E. Boone, R. P. Gunsalus, Disaggregation of Methanosarcina spp. and Growth as Single Cells at Elevated Osmolarity. *Appl Environ Microbiol*. **59**, 3832–3839 (1993).

3. W. W. Metcalf, J. K. Zhang, E. Apolinario, K. R. Sowers, R. S. Wolfe, A genetic system for Archaea of the genus Methanosarcina: Liposome-mediated transformation and construction of shuttle vectors. *Proceedings of the National Academy of Sciences*. **94**, 2626–2631 (1997).

4. D. E. Deatherage, J. E. Barrick, "Identification of Mutations in Laboratory-Evolved Microbes from Next-Generation Sequencing Data Using breseq" in *Engineering and Analyzing Multicellular Systems: Methods and Protocols*, L. Sun, W. Shou, Eds. (Springer, New York, NY, 2014; https://doi.org/10.1007/978-1-4939-0554-6_12), *Methods in Molecular Biology*, pp. 165–188.

5. A. P. Arkin, R. W. Cottingham, C. S. Henry, N. L. Harris, R. L. Stevens, S. Maslov, P. Dehal, D. Ware, F. Perez, S. Canon, M. W. Sneddon, M. L. Henderson, W. J. Riehl, D. Murphy-Olson, S. Y. Chan, R. T. Kamimura, S. Kumari, M. M. Drake, T. S. Brettin, E. M. Glass, D. Chivian, D. Gunter, D. J. Weston, B. H. Allen, J. Baumohl, A. A. Best, B. Bowen, S. E. Brenner, C. C. Bun, J.-M. Chandonia, J.-M. Chia, R. Colasanti, N. Conrad, J. J. Davis, B. H. Davison, M. DeJongh, S. Devoid, E. Dietrich, I. Dubchak, J. N. Edirisinghe, G. Fang, J. P. Faria, P. M. Frybarger, W. Gerlach, M. Gerstein, A. Greiner, J. Gurtowski, H. L. Haun, F. He, R. Jain, M. P. Joachimiak, K. P. Keegan, S. Kondo, V. Kumar, M. L. Land, F. Meyer, M. Mills, P. S. Novichkov, T. Oh, G. J. Olsen, R. Olson, B. Parrello, S. Pasternak, E. Pearson, S. S. Poon, G. A. Price, S. Ramakrishnan, P. Ranjan, P. C. Ronald, M. C. Schatz, S. M. D. Seaver, M. Shukla, R. A. Sutormin, M. H. Syed, J. Thomason, N. L. Tintle, D. Wang, F. Xia, H. Yoo, S. Yoo, D. Yu, KBase: The United States Department of Energy Systems Biology Knowledgebase. *Nat Biotechnol*. **36**, 566–569 (2018).

6. B. Langmead, S. L. Salzberg, Fast gapped-read alignment with Bowtie 2. *Nat Methods*. **9**, 357–359 (2012).

7. C. Trapnell, A. Roberts, L. Goff, G. Pertea, D. Kim, D. R. Kelley, H. Pimentel, S. L. Salzberg, J. L. Rinn, L. Pachter, Differential gene and transcript expression analysis of RNA-seq experiments with TopHat and Cufflinks. *Nat Protoc*. **7**, 562–578 (2012).

8. M. I. Love, W. Huber, S. Anders, Moderated estimation of fold change and dispersion for RNA-seq data with DESeq2. *Genome Biology*. **15**, 550 (2014).

9. D. D. Nayak, W. W. Metcalf, "Chapter Thirteen - Genetic techniques for studies of methyl-coenzyme M reductase from Methanosarcina acetivorans C2A" in *Methods in Enzymology*, F. Armstrong, Ed. (Academic Press, 2018; https://www.sciencedirect.com/science/article/pii/S0076687918304269), vol. 613 of *Enzymes of Energy Technology*, pp. 325–347.

10. A. Shevchenko, H. Tomas, J. Havli, J. V. Olsen, M. Mann, In-gel digestion for mass spectrometric characterization of proteins and proteomes. *Nat Protoc*. **1**, 2856–2860 (2006).

11. D. N. Mastronarde, Automated electron microscope tomography using robust prediction of specimen movements. *Journal of Structural Biology*. **152**, 36–51 (2005).

12. S. Q. Zheng, E. Palovcak, J.-P. Armache, K. A. Verba, Y. Cheng, D. A. Agard, MotionCor2: anisotropic correction of beam-induced motion for improved cryo-electron microscopy. *Nat Methods*. **14**, 331–332 (2017).

13. J. Zivanov, T. Nakane, B. O. Forsberg, D. Kimanius, W. J. Hagen, E. Lindahl, S. H. Scheres, New tools for automated high-resolution cryo-EM structure determination in RELION-3. *eLife*. **7**, e42166 (2018).

14. A. Punjani, J. L. Rubinstein, D. J. Fleet, M. A. Brubaker, cryoSPARC: algorithms for rapid unsupervised cryo-EM structure determination. *Nat Methods*. **14**, 290–296 (2017).

15. D. Asarnow, E. Palovcak, Y. Cheng, asarnow/pyem: UCSF pyem v0.5 (2019), , doi:10.5281/zenodo.3576630.

16. Y. Z. Tan, P. R. Baldwin, J. H. Davis, J. R. Williamson, C. S. Potter, B. Carragher, D. Lyumkis, Addressing preferred specimen orientation in single-particle cryo-EM through tilting. *Nat Methods*. **14**, 793–796 (2017).

17. D. Liebschner, P. V. Afonine, M. L. Baker, G. Bunkóczi, V. B. Chen, T. I. Croll, B. Hintze, L.-W. Hung, S. Jain, A. J. McCoy, N. W. Moriarty, R. D. Oeffner, B. K. Poon, M. G. Prisant, R. J. Read, J. S. Richardson, D. C. Richardson, M. D. Sammito, O. V. Sobolev, D. H. Stockwell, T. C. Terwilliger, A. G. Urzhumtsev, L. L. Videau, C. J. Williams, P. D. Adams, Macromolecular structure determination using X-rays, neutrons and electrons: recent developments in Phenix. *Acta Cryst D*. **75**, 861–877 (2019).

18. W. Grabarse, F. Mahlert, S. Shima, R. K. Thauer, U. Ermler, Comparison of three methyl-coenzyme M reductases from phylogenetically distant organisms: unusual amino acid modification, conservation and adaptation11Edited by R. Huber. *Journal of Molecular Biology*. **303**, 329–344 (2000).

19. J. Jumper, R. Evans, A. Pritzel, T. Green, M. Figurnov, O. Ronneberger, K. Tunyasuvunakool, R. Bates, A. Žídek, A. Potapenko, A. Bridgland, C. Meyer, S. A. A. Kohl, A. J. Ballard, A. Cowie, B. Romera-Paredes, S. Nikolov, R. Jain, J. Adler, T. Back, S. Petersen, D. Reiman, E. Clancy, M. Zielinski, M. Steinegger, M. Pacholska, T. Berghammer, S. Bodenstein, D. Silver, O. Vinyals, A. W. Senior, K. Kavukcuoglu, P. Kohli, D. Hassabis, Highly accurate protein structure prediction with AlphaFold. *Nature*. **596**, 583–589 (2021).

20. P. Emsley, B. Lohkamp, W. G. Scott, K. Cowtan, Features and development of *Coot*. *Acta Crystallogr D Biol Crystallogr*. **66**, 486–501 (2010).

21. E. F. Pettersen, T. D. Goddard, C. C. Huang, E. C. Meng, G. S. Couch, T. I. Croll, J. H. Morris, T. E. Ferrin, UCSF ChimeraX: Structure visualization for researchers, educators, and developers. *Protein Sci*. **30**, 70–82 (2021).